



HAL
open science

Spectral and modal energy transfer analyses of the discontinuous Galerkin Variational Multiscale approach

Fabio Naddei, Marta de La Llave Plata, Eric Lamballais

► **To cite this version:**

Fabio Naddei, Marta de La Llave Plata, Eric Lamballais. Spectral and modal energy transfer analyses of the discontinuous Galerkin Variational Multiscale approach. 2019. hal-02146622

HAL Id: hal-02146622

<https://hal.science/hal-02146622>

Preprint submitted on 4 Jun 2019

HAL is a multi-disciplinary open access archive for the deposit and dissemination of scientific research documents, whether they are published or not. The documents may come from teaching and research institutions in France or abroad, or from public or private research centers.

L'archive ouverte pluridisciplinaire **HAL**, est destinée au dépôt et à la diffusion de documents scientifiques de niveau recherche, publiés ou non, émanant des établissements d'enseignement et de recherche français ou étrangers, des laboratoires publics ou privés.

Spectral and modal energy transfer analyses of the discontinuous Galerkin Variational Multiscale approach

Fabio Naddei^a, Marta de la Llave Plata^a, Eric Lamballais^b

^aDepartment of Aerodynamics, Aeroelasticity and Acoustics, ONERA, France

^bInstitute PPRIME, Université de Poitiers, France

Abstract

In this work we perform *a-priori* analyses of the Discontinuous Galerkin (DG) Variational Multiscale (VMS) method for Large Eddy Simulation (LES). An analytical framework is introduced to study the ideal energy transfer between resolved and unresolved scales. The proposed framework is consistent with the discretization employed for the DG-LES simulations. The concept of modal eddy viscosity is also introduced which can be employed for the *a-priori* analysis of the DG-VMS method or spectral vanishing viscosity approaches. The developed framework is then applied to the analysis of the energy transfer in DG-LES by employing a DNS database of the Taylor-Green Vortex (TGV) at $Re = 5\,000$, $20\,000$ and $40\,000$. *A-priori* analyses are carried out for three variants of the DG-VMS approach: the small-small [1], Vreman [2], and all-all variants [3]. The performed analysis demonstrates that when the DG-LES resolution limit falls at the beginning of the dissipation range the assumption of large scales free of interaction with the unresolved scales is valid and the DG-VMS approach can replicate the ideal SGS dissipation spectrum. For coarser resolutions, typical of LES at high Reynolds numbers, the DG-VMS approach is unable to replicate the ideal energy transfer mechanism at the large-resolved scales. It is shown, *a-priori*, that a more accurate agreement can be obtained by employing a mixed Smagorinsky and DG-VMS approach with a fixed value of the scale-fraction parameter.

Keywords: High-order, discontinuous Galerkin, Variational Multiscale, *a-priori* analysis, spectral energy transfer

1. Introduction

Large Eddy Simulation (LES) is a well established methodology for the prediction of turbulent flows for applications ranging from fundamental research to industrial design [4, 5, 6]. The working principle of LES is to resolve only the large-scale turbulent eddies and model the effect of the unresolved scales by means of a subgrid-scale (SGS) closure, thereby reducing the computational cost of simulations with respect to Direct Numerical Simulation (DNS).

One of the fundamental traits of turbulence, that must be correctly reproduced by SGS models, is the physical mechanism of energy transfer between the resolved turbulent scales and the unresolved scales. This energy transfer mechanism can be studied by analysing the non-linear

URL: fabio.naddei@onera.fr (Fabio Naddei)

34 interaction of the full velocity field such as that obtained from DNS or by theoretical analyses by
35 employing an analytical energy spectrum.

36 Early theoretical analyses of the energy transfer mechanisms in turbulent flows were per-
37 formed by Heisenberg [7] and Kraichnan [8]. These studies involved the choice of an analytical
38 energy spectrum and an arbitrary convolution filter to separate resolved and unresolved scales
39 and evaluate the corresponding non linear interactions and energy transfer. The energy transfer
40 mechanism was represented by means of an additional *spectral eddy viscosity* acting on the re-
41 solved modes. Kraichnan [8] employed a sharp cut-off filter in Fourier space to separate resolved
42 and unresolved scales in theoretical turbulence characterized by an infinite inertial range (i. e. as-
43 suming infinite Reynolds number). Under these conditions, Kraichnan identified the presence
44 of a cusp in the spectral eddy viscosity, near the cut-off, and a plateau at lower wavenumbers,
45 which is a manifestation of the significant interaction between the unresolved scales and the large
46 resolved scales away from the cut-off.

47 *A-priori* numerical analyses were carried out by Domaradzki et al. [9] based on DNS of the
48 Taylor-Green Vortex (TGV) flow at $Re = 3\,000$ by applying a sharp spectral filter to define the
49 ideal LES solution. This work confirmed the presence of the cusp of the spectral eddy viscosity
50 near the cut-off. However, differently from the studies of Kraichnan, a negligible energy transfer
51 was observed at relatively lower wavenumbers. A similar result was observed by McComb and
52 Young [10] who analysed the spectral eddy viscosity for homogeneous isotropic turbulence at
53 microscale Reynolds number $Re_\lambda = 190$. In their work a plateau in the eddy viscosity was ob-
54 served only for the coarsest resolution, indicating a negligible interaction between large resolved
55 and unresolved scales. In contrast, Métais and Lesieur [11] identified a plateau in the spectral
56 eddy viscosity evaluated from an LES of homogeneous isotropic turbulence at infinite Reynolds
57 number.

58 Using *a-priori* testing, the ideal energy transfer and the effective eddy viscosity obtained
59 by applying the LES filter to DNS data can be employed to evaluate SGS models and aid in
60 their improvement. As an example, the Smagorinsky model [12], still widely employed due to
61 its simplicity and robustness, has been shown in *a-priori* analyses to be overdissipative on the
62 large-scale structures, confirming the observations from *a-posteriori* tests [13]. Using the same
63 approach, it has been shown that even though its dynamic variant by Germano et al. [14] is able
64 to provide the correct global SGS dissipation and near-wall scaling, it fails to reproduce the ideal
65 energy transfer spectrum (also called SGS dissipation spectrum). Indeed, it introduces an insuf-
66 ficient amount of dissipation at high frequencies while exhibiting an overdissipative behaviour at
67 low frequencies as shown e. g. by Hughes et al. [15].

68 A number of new SGS models have been developed with the aim of reducing these short-
69 comings of traditional LES techniques. One such model is the Variational Multiscale (VMS)
70 approach proposed by Hughes et al. [16]. The VMS approach advocates the strict separation of
71 the resolved velocity field into a large-scale component, containing the largest coherent struc-
72 tures of the flow, and a small-scale component by means of a high-pass projection filter. The
73 model then relies on the spectral gap assumption such that the large resolved scales are assumed
74 to be virtually free of SGS dissipation. Thus the model (e. g. the Smagorinsky model or its
75 dynamic version) only acts on the small-scale resolved component of the velocity field. This
76 approach therefore mimics the ideal energy transfer mechanism as described by Domaradzki
77 et al. [9]. The VMS approach, originally developed in the context of stabilized finite element
78 (FE) and spectral methods, has demonstrated very accurate results in the simulation of several
79 turbulent flow configurations and has since been extended to finite volume (FV) and spectral
80 element type methods such as the discontinuous Galerkin (DG) method. We refer to the reviews

81 of Gravemeier [17], Ahmed et al. [18] and Rasthofer and Gravemeier [19] for an overview of the
82 VMS approach and several variants that have been proposed by other authors.

83 The combination of the VMS approach with DG methods in particular presents several prop-
84 erties which are of great interest for the improvement of the quality and efficiency of LES [20].
85 The DG methods have rapidly gained popularity for scale-resolving simulations due to their ex-
86 cellent scalability and their ability to achieve high-order accuracy on general meshes [21]. The
87 variational framework on which these methods rely allows for the local separation of scales us-
88 ing polynomial basis functions, which can be employed for multi-level methods and the VMS
89 approach. In contrast to the spectral method, the DG framework allows for the efficient separa-
90 tion of scales even while working on completely unstructured meshes without requiring complex
91 spatial filters. Moreover, the high-order polynomial representation of the solution allows for a
92 higher flexibility in the decomposition into large and small scale components, as compared to
93 FV and low order FE methods. Finally, the use of discontinuous solution spaces allows for the
94 straightforward local adaptation of the scale-separation operator.

95 There are however still several open questions which require specific analysis in the context
96 of the DG-VMS method. These are: the effect of the LES filter on the effective eddy viscosity,
97 the effect of the scale-separation operator and the calibration of the coefficient involved in the
98 SGS model. While these questions are still the subject of current research in the context of
99 the DG-VMS approach, several studies have been already carried out in the context of standard
100 LES approaches based on convolution filters. The main conclusions of these works are briefly
101 outlined below.

102 *The effect of the LES filter.* Leslie and Quarini [22] performed theoretical analyses by consider-
103 ing an infinite inertial range and a Gaussian filter. Their results demonstrated that, in contrast to
104 what is obtained for a sharp spectral filter, the use of a Gaussian filter leads to an spectral eddy
105 viscosity characterized by a plateau from low to high wavenumbers and a sharp decay as the
106 wavenumber approaches $1/\Delta$ (Δ being the filter width). Moreover, in the case of a production-
107 type spectrum, the shape of the ideal eddy viscosity strongly depends on the ratio between the
108 LES cut-off frequency k_c and that corresponding to the energy production phenomena. Similar
109 conclusions can be drawn from the work of Cerutti et al. [23] who evaluated the eddy viscosity
110 from experimental measurements corresponding to the use of a mixed filter (spectral cut-off in
111 one direction and top-hat filter in the other two directions). The outcome of this study led the
112 authors to conclude that the use of a mixed viscosity-hyperviscosity model can improve the accu-
113 racy of LES simulations. More recently Lamballais et al. [24] have evaluated the eddy viscosity
114 from the DNS of the TGV configuration at $Re = 20\,000$ and observed the presence of the plateau
115 described by Kraichnan [8] employing a spectral cut-off filter.

116 It appears, therefore, that the validity of the spectral gap assumption needs to be carefully
117 analysed depending on the LES filter employed in the simulation. The extension of these analyses
118 to the case of the DG-VMS approach presents additional complications as the DG-projection
119 filter is not a convolution filter (as explained in Sec. 2). Thus this topic deserves special attention.

120 *The effect of the high-pass filter.* The second open question is the effect of the high-pass filter
121 on the quality of the VMS model. As regards the choice of the cut-off frequency \bar{k} associated
122 with the high-pass filter, in actual simulations, this parameter is often selected heuristically or by
123 trying to match reference results. In early numerical experiments, Hughes et al. [16] and Hughes
124 et al. [1] have used a high-pass spectral filter with \bar{k} corresponding to a scale-fraction parameter
125 $\beta = \bar{k}/k_c$ equal to 0.59 and 0.5, respectively, when employing the VMS approach with constant

126 model coefficient. In later works Hughes et al. [15] employed a scale-fraction parameter $\beta = 0.5$
127 for the VMS approach based on the dynamic Germano procedure for the determination of the
128 model constant. Holmen et al. [25] carried out a sensitivity analysis for the LES of the turbulent
129 channel flow. The authors showed that the use of the dynamic procedure reduces the sensitivity
130 of the VMS-LES to the scale-fraction parameter and optimal results were obtained for $\beta \approx 0.5$.
131 In contrast, for the static variants optimal results were obtained for $\beta \approx 0.7$ and the quality of the
132 solution quickly deteriorated for other values. Ramakrishnan and Collis [26] have shown that the
133 optimal scale-fraction parameter might depend on the flow considered and resolution available.
134 It was observed that the optimal high-pass filter length can be related to the characteristic length
135 of coherent structures of the flow. However they remarked that the small-scale space should
136 contain at least 50% – 60% of all modes to provide high quality first and second-order statistics.

137 The effect of the type of the high-pass filter in VMS was also analysed by Sagaut and Lev-
138 asseur [27] and Meyers and Sagaut [28]. It was observed that the sharp-cut off filter (orthogonal
139 in Fourier space) can provide an overdissipative behaviour at high frequencies leading to a bot-
140 tleneck effect and the generation of a middle-wavenumber pile-up. Moreover, a discrete jump
141 might appear in the energy spectrum near the high-pass filter cut-off (as observed by Meyers and
142 Sagaut [28]). The use of a non-orthogonal high-pass filter (e. g. Gaussian filter) led to improved
143 results by rendering all scales sensitive to the subgrid closure. Similar results were reported
144 by Meyers and Sagaut [28] who further noted a reduced dependency on β when employing a
145 Gaussian filter.

146 *Calibration of the SGS model constant.* As regards the value of the constant involved in the VMS
147 model, a calibration has been derived by Hughes et al. [16] using the procedure due to Lilly [29].
148 The procedure assumes an infinite Reynolds number (infinite inertial range) and the calibration
149 was obtained considering an isotropic sharp spectral filter for both the LES and high-pass filters.
150 The most comprehensive work on the calibration of the model constant for the VMS approach is
151 however the study by Meyers and Sagaut [30]. One of the most important results of this research
152 is that the optimal model coefficient strongly depends on the choice of LES and high-pass filter.
153 Moreover, the authors have provided an analytical framework for the evaluation of the optimal
154 model coefficient in the case of convolution filters. As already mentioned, the DG-projection
155 filter is not a convolution filter and therefore special care is required to extend the conclusions of
156 these works.

157 The studies cited above clearly outline that the performance of the VMS approach is strongly
158 influenced by a number of parameters primarily associated with the LES and high-pass filters.
159 Therefore the systematic and robust application of the DG-VMS approach can be improved by
160 analysing these questions in the context of the DG-projection filter as both the LES filter and
161 scale-separation operator. We analyse for this purpose the effect of the DG-LES filter on the
162 ideal energy transfer and the validity of the assumption of absence of SGS dissipation acting on
163 the largest resolved scales. The accuracy of the DG-VMS approach and the associated high-pass
164 filter in replicating the ideal energy transfer will then be considered with the objective of identi-
165 fying guidelines for the selection of the scale-fraction parameter.

166 This work is therefore organized as follows. In Section 2 the DG-filter and the ideal DG-
167 LES solution are discussed. Their definition is then employed in Sections 3 and 4 to extend
168 the energy transfer analysis framework to the context of DG-LES. The presented framework is
169 then applied in Section 5 to a DNS database of the TGV configuration at $Re = 5\,000$, $20\,000$ and
170 $40\,000$. Obtained results are then compared in Section 6 to the energy transfer and eddy viscosity
171 provided by the DG-VMS approach. Finally conclusions are presented in Section 7.

172 **2. The ideal DG-LES solution**

173 *A-priori* testing can provide valuable information about the accuracy of LES modeling ap-
 174 proaches. The central question with this type of analysis is the definition of an appropriate ideal
 175 LES solution, which in the general case is not straightforward. It is, however, essential to answer
 176 this question, as the way in which this ideal solution is defined has a direct impact on the way
 177 the ideal SGS quantities are computed.

178 The classical approach consists in defining the ideal LES solution as the spatially filtered
 179 DNS solution. For this purpose convolution filters are conventionally employed such that for any
 180 function f we define the filtered function $\bar{f}(x) := \int_{\Omega} G(x - \xi) f(\xi) d\xi$ with $G(x - \xi)$ being the filter
 181 kernel. The convolution filter can be applied to the Navier-Stokes (NS) equations such that the
 182 ideal LES solution satisfies the filtered NS equations in their strong form. One of the advantages
 183 of this approach is that the application of the convolution filter can be expressed in the Fourier
 184 space as $\widehat{\bar{f}}(k) = \widehat{G}(k) \widehat{f}(k)$ where $\widehat{(\cdot)}$ denotes the Fourier transform and it is easy to demonstrate
 185 that the convolution filter commutes with spatial derivatives. This approach however entirely
 186 ignores the details of the discretization employed and the fact that the LES solution so defined
 187 might not be an admissible solution of the considered discrete problem. Thus this approach
 188 presents serious limitations when extending the results of *a-priori* and theoretical analyses to FV
 189 and FE type methods.

190 A second approach has been proposed by Pope [31], in which the LES solution is conceived
 191 as the projection of the DNS solution onto a set of local basis functions. It has been shown by
 192 Vreman [32] that an arbitrary orthogonal projection operator can be reformulated as a kernel filter
 193 such that for any function f we can indicate its projection as $f_h(x) := \mathbb{P}_h[f] = \int_{\Omega} K_p(x, \xi) f(\xi) d\xi$.
 194 The use of a non uniform filter kernel $K_p(x, \xi)$ implies that in general the projection operation
 195 and differentiation do not commute. For this reason the closure problem needs to be redefined
 196 employing the semidiscrete weak form of the equations as described by Pope [31] and in the
 197 context of the VMS approach (e.g. [33]).

198 This methodology provides a definition of the ideal resolved field which is consistent with
 199 the employed numerical discretization. Following this approach Beck et al. [34] have defined the
 200 ideal DG-LES solution as the L^2 -projection of the DNS solution on the discretization space and
 201 identified the ideal subgrid stress to develop a Deep Neural Network turbulence model. Similarly
 202 van der Bos and Geurts [35] have defined the ideal DG-LES solution by means of a face-based
 203 projection to perform a systematic analysis of computational errors of DG-FEM for LES.

204 The use of a projection type filter however can introduce significant aliasing errors at wavenum-
 205 bers close to the grid cut-off, producing unphysical reference data. This is a direct consequence
 206 of the approximation properties of polynomial basis functions (see [36]).

207 In this work we propose to employ an alternative approach in which the ideal DG-LES so-
 208 lution is defined as the result of the application of two successive filtering operations. A first
 209 convolution filter is applied to the DNS data which filters out frequencies beyond the LES grid
 210 cut-off. Next, a L^2 -projection of this filtered field is performed on the hp -discretization space
 211 (referred to in the following as DG-projection). This procedure reduces considerably the aliasing
 212 errors introduced by Pope's approach, while allowing the inclusion in the analysis of the effect
 213 of the hp -discretization associated with the adopted numerical method.

214 The following section provides a formal framework for the definition of the ideal DG-LES
 215 solution as described above and the expression of the corresponding ideal SGS energy transfer.

216 **3. The DG-LES framework and the ideal energy transfer**

217 The N-S equations for an incompressible flow read

$$\frac{\partial \mathbf{u}}{\partial t} + \nabla \cdot \mathcal{F}_c(\mathbf{u}, q) + \nabla \cdot \mathcal{F}_v(\mathbf{u}, \nabla \mathbf{u}) = 0, \quad \forall \mathbf{x} \in \Omega, t \geq 0, \quad (1)$$

$$\nabla \cdot \mathbf{u} = 0, \quad (2)$$

219 where \mathbf{u} is the velocity field, q is the pressure, and \mathcal{F}_c and \mathcal{F}_v are the convective and viscous
220 fluxes, defined respectively as

$$\mathcal{F}_c(\mathbf{u}, q) = \mathbf{u} \otimes \mathbf{u} + qI, \quad (3)$$

$$\mathcal{F}_v(\mathbf{u}, \nabla \mathbf{u}) = \nu(\nabla \mathbf{u} + (\nabla \mathbf{u})^T). \quad (4)$$

221 We define Ω_h to be a shape regular partition of Ω into N non-overlapping, non-empty ele-
222 ments of characteristic size h and we further define the broken Sobolev space $S_h^p := \{\phi \in L^2(\Omega_h) :$
223 $\phi|_K \in \mathcal{P}^p(K), \forall K \in \Omega_h\}$ to be the space of piecewise polynomials of partial degree at most p .
224 Then we indicate as $f_h := \mathbb{P}_{S_h^p}[f]$ the projection of any function f on the hp -discretization defined
225 by the space S_h^p .

226 Following the approach described in the previous section, we define the ideal DG-LES so-
227 lution as $\bar{\mathbf{u}}_h := \mathbb{P}_{S_h^p}[\bar{\mathbf{u}}]$, which is the result of the successive application to the velocity field \mathbf{u}
228 of a convolution filter and the DG-projection filter defined by the space S_h^p . The convolution
229 filter employed in this work is a sharp spectral anisotropic filter with expression in spectral space
230 $G(\mathbf{k}) = H(k_{\text{DG}} - \|\mathbf{k}\|_\infty)$ where $k_{\text{DG}} = \pi(p + 1)/h$ and H is the Heaviside function.

231 Applying the convolution and DG-projection filter to Eq. (1), we derive the evolution equa-
232 tions for the ideal DG-LES solution

$$\begin{aligned} \frac{\partial}{\partial t} \int_{\Omega_h} \bar{\mathbf{u}}_h \phi \, d\mathbf{x} + \sum_K \left[\int_{\partial K} \bar{\mathcal{F}}_c(\mathbf{u}, q) \cdot \mathbf{n}^+ \phi^+ \, d\sigma - \int_K \bar{\mathcal{F}}_c(\mathbf{u}, q) \cdot \nabla \phi \, d\mathbf{x} \right. \\ \left. + \int_{\partial K} \bar{\mathcal{F}}_v(\mathbf{u}, \nabla \mathbf{u}) \cdot \mathbf{n}^+ \phi^+ \, d\sigma - \int_K \bar{\mathcal{F}}_v(\mathbf{u}, \nabla \mathbf{u}) \cdot \nabla \phi \, d\mathbf{x} \right] = 0, \quad \forall \phi \in S_h^p, \end{aligned} \quad (5)$$

233 where we have used the commutation property of the convolution filter with spatial derivatives
234 and the definition of the L^2 -projection, which implies, $\int_{\Omega_h} (\bar{\mathbf{u}} - \bar{\mathbf{u}}_h) \phi = 0, \forall \phi \in S_h^p$.

235 The DG-LES equations can now be defined by rewriting Eq. (5) as

$$\begin{aligned} \frac{\partial}{\partial t} \int_{\Omega_h} \bar{\mathbf{u}}_h \phi \, d\mathbf{x} + \underbrace{\sum_K \left[\int_{\partial K} \mathbf{h}_c(\bar{\mathbf{u}}_h^+, \bar{q}_h^+, \bar{\mathbf{u}}_h^-, \bar{q}_h^-, \mathbf{n}^+) \phi^+ \, d\sigma - \int_K \mathcal{F}_c(\bar{\mathbf{u}}_h, \bar{q}_h) \cdot \nabla \phi \, d\mathbf{x} \right]}_{\mathcal{L}_c(\bar{\mathbf{u}}_h, \bar{q}_h, \phi)} + \\ \underbrace{\sum_K \left[\int_{\partial K} \mathbf{h}_v(\bar{\mathbf{u}}_h^+, \bar{\mathbf{u}}_h^-, \mathbf{n}^+) \phi^+ \, d\sigma - \int_K \mathcal{F}_v(\bar{\mathbf{u}}_h, \nabla \bar{\mathbf{u}}_h) \cdot \nabla \phi \, d\mathbf{x} \right]}_{\nu \mathcal{L}_v(\bar{\mathbf{u}}_h, \phi)} + \mathcal{R}(\mathbf{u}, \bar{\mathbf{u}}_h, \phi) = 0, \quad \forall \phi \in S_h^p, \end{aligned} \quad (6)$$

236 where \mathbf{h}_c and \mathbf{h}_v are the convective and diffusive numerical fluxes and f^+ and f^- indicate the
 237 trace of any function f on the element's boundary ∂K .

238 In Eq. (6), $\mathcal{R}(\mathbf{u}, \bar{\mathbf{u}}_h, \phi)$ is the subgrid-scale residual representing the effect of the unresolved
 239 scales $\mathbf{u} - \bar{\mathbf{u}}_h$ on the resolved field, which can be obtained by comparing Eq. (5) and Eq. (6). Note
 240 that, as the DG-projection filter does not commute with spatial derivation nor the convolution
 241 filter, in general both the pressure and viscous terms contribute to the subgrid-scale residual. In
 242 this work, however, we assume that the SGS term is dominated by convective effects thus the
 243 contribution of the viscous and pressure terms is neglected. This leads to the following form for
 244 the subgrid residual,

$$\begin{aligned} \mathcal{R}(\mathbf{u}, \bar{\mathbf{u}}_h, \phi) \approx & \sum_K \left[\int_K (\mathcal{F}_c(\bar{\mathbf{u}}_h) - \overline{\mathcal{F}_c(\mathbf{u})}) \cdot \nabla \phi \, d\mathbf{x} \right. \\ & \left. - \int_{\partial K} (\mathbf{h}_c(\bar{\mathbf{u}}_h^+, \bar{\mathbf{u}}_h^-, \mathbf{n}^+) - \overline{\mathcal{F}_c(\mathbf{u})} \cdot \mathbf{n}^+) \phi^+ \, d\sigma \right]. \end{aligned} \quad (7)$$

245 Indicating as $\{\psi_K^1 \dots \psi_K^{N_p}\} \in \mathcal{P}^p(K)$ an orthonormal basis for $\mathcal{P}^p(K)$ with $\psi_K^i(\mathbf{x}) = 0, \forall \mathbf{x} \in$
 246 $K', K' \neq K$, the solution $\bar{\mathbf{u}}_h$ is expressed as a linear combination of the basis functions such
 247 that

$$\bar{\mathbf{u}}_h(\mathbf{x}, t) = \sum_K \sum_{i=1}^{N_p} \widetilde{\bar{\mathbf{u}}}_h^{i,K}(t) \psi_K^i(\mathbf{x}), \quad \forall \mathbf{x} \in \Omega_h, \quad (8)$$

248 where the modal coefficients $\widetilde{\bar{\mathbf{u}}}_h^{i,K}$ obey the following equation derived from Eq. (6)

$$\frac{\partial \widetilde{\bar{\mathbf{u}}}_h^{i,K}}{\partial t} + \mathcal{L}_c(\bar{\mathbf{u}}_h, \bar{q}_h, \psi_K^i) + \nu \mathcal{L}_v(\bar{\mathbf{u}}_h, \psi_K^i) + \mathcal{R}(\mathbf{u}, \bar{\mathbf{u}}_h, \psi_K^i) = 0, \quad \forall K \in \Omega_h, \forall i = 1 \dots N_p. \quad (9)$$

249 These equations can be combined to rewrite the semidiscrete DG-LES equations (6) as

$$\frac{\partial \bar{\mathbf{u}}_h}{\partial t} + \mathcal{L}_c(\bar{\mathbf{u}}_h, \bar{q}_h) + \nu \mathcal{L}_v(\bar{\mathbf{u}}_h) + \mathbf{R}(\mathbf{u}, \bar{\mathbf{u}}_h) = 0, \quad (10)$$

where

$$\mathcal{L}_c := \sum_K \sum_i \mathcal{L}_c(\bar{\mathbf{u}}_h, \bar{q}_h, \psi_K^i) \psi_K^i, \quad (11)$$

$$\mathcal{L}_v := \sum_K \sum_i \mathcal{L}_v(\bar{\mathbf{u}}_h, \psi_K^i) \psi_K^i, \quad (12)$$

$$\mathbf{R} := \sum_K \sum_i \mathcal{R}(\mathbf{u}, \bar{\mathbf{u}}_h, \psi_K^i) \psi_K^i. \quad (13)$$

250 This leads to the following equation for the evolution of the energy associated to each wavenum-
 251 ber \mathbf{k} of the resolved scales as

$$\frac{\partial E(\mathbf{k})}{\partial t} + \widehat{\bar{\mathbf{u}}}_h(\mathbf{k}) \cdot \widehat{\mathcal{L}}_c(\mathbf{k}) + \nu \widehat{\bar{\mathbf{u}}}_h(\mathbf{k}) \cdot \widehat{\mathcal{L}}_v(\mathbf{k}) + \widehat{\bar{\mathbf{u}}}_h(\mathbf{k}) \cdot \widehat{\mathbf{R}}(\mathbf{k}) = 0. \quad (14)$$

252 The ideal energy transfer from the resolved modes of wavenumber k to all unresolved scales can
 253 therefore be obtained from the subgrid residual as

$$T_{sgs}(k) = \sum_{\|\mathbf{k}\|=k} \widehat{\bar{\mathbf{u}}}_h(\mathbf{k}) \cdot \widehat{\mathbf{R}}(\mathbf{k}). \quad (15)$$

254 Positive values of T_{sgs} correspond to kinetic energy being transferred from resolved to unre-
 255 solved scales, whereas negative values correspond to energy being transferred from unresolved
 256 to resolved scales, commonly indicated as backscatter.

257 Note that the use of the DG-projection filter introduces discontinuities in the filtered velocity
 258 field that need to be taken into account. It also requires the definition of the numerical flux \mathbf{h}_c
 259 that appears in the surface integral in Eq. (7). The subgrid stress thus depends in general on
 260 both, the definition of the filter and the choice of this numerical flux. While this choice might
 261 appear arbitrary, it reflects the notion that the subgrid term which needs to be modelled must take
 262 into account the choice of the numerical discretization and the numerical dissipation thereby
 263 introduced.

264 In the *a-priori* analyses presented in the following, we are interested in investigating the ideal
 265 SGS dissipation in absence of dissipation introduced by the discretization of the convective flux.
 266 For this purpose we consider a central flux $\mathbf{h}_c(\bar{\mathbf{u}}_h^+, \bar{\mathbf{u}}_h^-, \mathbf{n}^+) = \frac{1}{2}(\mathcal{F}_c(\bar{\mathbf{u}}_h^+) + \mathcal{F}_c(\bar{\mathbf{u}}_h^-)) \cdot \mathbf{n}^+$.

267 3.1. The modal energy transfer and eddy viscosity

268 The analysis presented up to this point represents an extension of the classical energy transfer
 269 spectral/Fourier analysis. In the context of the DG method useful information can be extracted
 270 by performing this analysis in the modal/polynomial space. For this purpose, let us consider now
 271 Ω to be a cubic domain with Ω_h being a uniform Cartesian grid. We further consider a basis
 272 for S_h^p which is formed by the tensor product of normalized Legendre polynomials of maximum
 273 degree p . We indicate as $\psi_K^{\mathbf{m}}$ the generic element of this basis such that $\mathbf{m} = (m_x, m_y, m_z)$ and

$$\psi_K^{\mathbf{m}} = l^{m_x} \left(\frac{x-x_{K,c}}{h/2} \right) l^{m_y} \left(\frac{y-y_{K,c}}{h/2} \right) l^{m_z} \left(\frac{z-z_{K,c}}{h/2} \right) \quad (16)$$

274 where $x_{K,c}$, $y_{K,c}$ and $z_{K,c}$ are the coordinates of the barycenter of K and l^i is the i -th Legendre
 275 polynomial normalized such that $\|\psi_K^{\mathbf{m}}\|_{L^2(\Omega_h)} = 1$.

276 We then define $W_h^m = \text{span} \{ \psi_K^{\mathbf{m}}, \forall K \in \Omega_h, m - \frac{1}{2} < \|\mathbf{m}\| \leq m + \frac{1}{2} \}$, we call m the mode-number
 277 and define $\mathbb{P}_{W_h^m}[\bar{\mathbf{u}}_h]$ as the component of the DG-LES solution $\bar{\mathbf{u}}_h$ of mode-number m and the
 278 modal energy spectrum as

$$\tilde{E}(m) = \frac{1}{2} \int_{\Omega_h} \mathbb{P}_{W_h^m}[\bar{\mathbf{u}}_h] \cdot \mathbb{P}_{W_h^m}[\bar{\mathbf{u}}_h] \, d\mathbf{x} \quad (17)$$

279 As $\int_{\Omega_h} (\mathbb{P}_{W_h^m}[\bar{\mathbf{u}}_h] - \bar{\mathbf{u}}_h) \phi \, d\mathbf{x} = 0$, $\forall \phi \in W_h^m$ and $W_h^m \subset S_h^p$, from Eq. (5) we can write

$$\int_{\Omega_h} \frac{\partial}{\partial t} \mathbb{P}_{W_h^m}[\bar{\mathbf{u}}_h] \phi \, d\mathbf{x} + \mathcal{L}_c(\bar{\mathbf{u}}_h, \phi) + \nu \mathcal{L}_v(\bar{\mathbf{u}}_h, \phi) + \mathcal{R}(\mathbf{u}, \bar{\mathbf{u}}_h, \phi) = 0, \quad \forall \phi \in W_h^m, \quad (18)$$

280 and it can be immediately obtained that

$$\frac{\partial \tilde{E}(m)}{\partial t} + \mathcal{L}_c(\bar{\mathbf{u}}_h, \mathbb{P}_{W_h^m}[\bar{\mathbf{u}}_h]) + \nu \mathcal{L}_v(\bar{\mathbf{u}}_h, \mathbb{P}_{W_h^m}[\bar{\mathbf{u}}_h]) + \mathcal{R}(\mathbf{u}, \bar{\mathbf{u}}_h, \mathbb{P}_{W_h^m}[\bar{\mathbf{u}}_h]) = 0 \quad (19)$$

281 Thus the modal energy transfer from the resolved scales of mode-number m to the unresolved
 282 scales can be evaluated as

$$\tilde{T}_{sgs}(m) := \mathcal{R}(\mathbf{u}, \bar{\mathbf{u}}_h, \mathbb{P}_{W_h^m}[\bar{\mathbf{u}}_h]) \quad (20)$$

283 It is can be easily shown that Eq. (20) can be rewritten as

$$\tilde{T}_{sgs}(m) = \sum_{K \in \Omega_h} \sum_{m - \frac{1}{2} < |\mathbf{m}| \leq m + \frac{1}{2}} \widetilde{\mathbf{u}}_h^{\mathbf{m}, K} \cdot \mathcal{R}(\mathbf{u}, \bar{\mathbf{u}}_h, \psi_K^{\mathbf{m}}), \quad (21)$$

284 with $\widetilde{\mathbf{u}}_h^{\mathbf{m}, K} = \int_{\Omega_h} \bar{\mathbf{u}}_h \psi_K^{\mathbf{m}} d\mathbf{x}$, which closely resembles Eq. (15) obtained in Fourier space. We thus
285 introduce the concept of a modal eddy viscosity, defined as

$$\tilde{\nu}_e(m) := \frac{\mathcal{R}(\mathbf{u}, \bar{\mathbf{u}}_h, \mathbb{P}_{W_h^m}[\bar{\mathbf{u}}_h])}{\mathcal{L}_\nu(\bar{\mathbf{u}}_h, \mathbb{P}_{W_h^m}[\bar{\mathbf{u}}_h])}, \quad (22)$$

286 which can be interpreted as an additional eddy viscosity which acts on the resolved modes simi-
287 larly to the spectral eddy viscosity defined by Kraichnan [8].

288 We point out that neither the modal energy transfer nor the modal eddy viscosity necessarily
289 have a physical meaning. This methodology is however useful as it can be directly compared
290 to the VMS approach and LES models based on a spectral vanishing viscosity such as that pro-
291 posed by Karamanos and Karniadakis [37]. In the context of DG methods, these approaches are
292 based on modifying the modal energy transfer or eddy viscosity provided by an SGS model as a
293 function of \mathbf{m} . A similar energy transfer analysis has already been employed by Oberai et al. [38]
294 to perform *a-priori* analyses of the VMS approach based on a FE method.

295 In the following, the modal eddy viscosity is presented normalized by the laminar viscosity

$$\tilde{\nu}_e^\dagger(m) := \frac{\tilde{\nu}_e(m)}{\nu}. \quad (23)$$

296 We point out that Eq. (22) depends on the discretization of the viscous terms. Therefore it
297 provides the modal eddy viscosity which must be provided by the SGS model employing a cho-
298 sen discretization. This approach highlights the relevance of taking into account the dissipation
299 properties of the numerical scheme used for the discretization of the model term. In Sec. 5 and 6
300 results will be presented which are based on the BR1 scheme [39] and the BR2 scheme [40].

301 4. The DG-LES modelling and the DG-VMS approach

302 Starting from Eq. (6), the effect of the subgrid scales can be approximated by a model term
303 that depends only on the resolved field

$$\mathcal{R}(\mathbf{u}, \bar{\mathbf{u}}_h, \phi) \approx \mathcal{L}_m(\bar{\mathbf{u}}_h, \phi). \quad (24)$$

304 One common approach to formulate SGS models for DG methods is to discretize LES models
305 derived in the continuous framework, such as those relying on an eddy-viscosity approach like
306 the Smagorinsky model.

307 For the Smagorinsky model, a SGS flux is introduced in the filtered NS equations which takes
308 the form

$$\mathcal{F}_m = 2\nu_s(\nabla\mathbf{u})S(\nabla\mathbf{u}) \quad \text{with} \quad \nu_s(\nabla\mathbf{u}) = (C_s\Delta)^2 \|S(\nabla\mathbf{u})\|, \quad (25)$$

309 where $S = \frac{1}{2}(\nabla\mathbf{u} + \nabla\mathbf{u}^T)$ is the strain rate tensor, with norm $\|S\| = \sqrt{2S_{ij}S_{ij}}$. The Smagorinsky
310 constant C_s has values between 0.1 and 0.2, and Δ is the filter width which in the DG framework
311 can be defined as $\Delta = h/(p+1)$.

312 By applying the same numerical treatment used for the viscous fluxes, the DG-LES model
313 term can be written as,

$$\mathcal{L}_m(\bar{\mathbf{u}}_h, \phi) = \sum_K \left[\int_{\partial K} \mathbf{h}_m(\bar{\mathbf{u}}_h^+, \bar{\mathbf{u}}_h^-, \mathbf{n}^+) \phi^+ d\sigma - \int_K \mathcal{F}_m(\bar{\mathbf{u}}_h) \nabla \phi d\mathbf{x} \right], \quad \forall \phi \in S_h^p, \quad (26)$$

314 where \mathbf{h}_m is the model numerical flux.

315 Following the approach presented above (see Sec. 3.1), the modelled spectral energy transfer
316 can therefore be evaluated as

$$T_m(k) = \sum_{\|\mathbf{k}\|=k} \widehat{\bar{\mathbf{u}}}_h(\mathbf{k}) \cdot \widehat{L}_m(\mathbf{k}) \quad \text{with} \quad L_m := \sum_K \sum_{\mathbf{m}} \mathcal{L}_m(\bar{\mathbf{u}}_h, \psi_K^{\mathbf{m}}) \psi_K^{\mathbf{m}}, \quad (27)$$

317 and the modelled modal energy transfer and eddy viscosity take the form

$$\widetilde{T}_m(m) := \mathcal{L}_m(\bar{\mathbf{u}}_h, \mathbb{P}_{W_h^m}[\bar{\mathbf{u}}_h]), \quad \text{and} \quad \widetilde{\nu}_m^\dagger(m) := \frac{\mathcal{L}_m(\bar{\mathbf{u}}_h, \mathbb{P}_{W_h^m}[\bar{\mathbf{u}}_h])}{\nu \mathcal{L}_\nu(\bar{\mathbf{u}}_h, \mathbb{P}_{W_h^m}[\bar{\mathbf{u}}_h])}. \quad (28)$$

318 The VMS approach is based on the separation of the resolved scales into large and small
319 resolved scales by means of a projection filter. To this end, we separate the solution space into
320 a large-scale space $V^L := \bigcup_{m \leq p_L} W_h^m$ and a small-scale space $V^S := S_h^p \setminus V^L$, where p_L is the
321 so-called scale-separation parameter and we indicate as $\beta = (p_L + 1)/(p + 1)$ the scale-fraction
322 parameter.¹

323 The original formulation of the VMS approach proposed by Hughes et al. [16] relies on two
324 assumptions: the absence of energy transfer between the large resolved and the unresolved scales
325 and the fact that the SGS model should be evaluated from the small-resolved scales.

326 This leads to a model term which takes the form

$$(\nabla \cdot \mathcal{F}_m(\bar{\mathbf{u}}_h))_{s-s} = \mathbb{P}_{V^S} [\nabla \cdot (2\nu_s(\mathbb{P}_{V^S}[\nabla \bar{\mathbf{u}}_h])S(\mathbb{P}_{V^S}[\nabla \bar{\mathbf{u}}_h]))]. \quad (29)$$

327 This approach is commonly referred to as the *small-small* approach, as both the eddy viscosity
328 and the strain rate tensor in the model term are computed directly from the small resolved scales.
329 The outer filter operation restricts the action of the LES model only to the small-scale solu-
330 tion corresponding to mode-numbers higher than the scale-separation parameter. It corresponds
331 therefore to the assumption $\widetilde{T}_{sgs}(m) \approx 0$ and $\widetilde{\nu}_{sgs} \approx 0$ for $m \leq p_L$.

332 We point out once more that the L^2 -projection and differentiation do not commute, thus
333 the order of the operations is important in the definition of the model term. In particular, we
334 remark that while the effect of the model is applied to the small-scale solution, the model flux is
335 computed from the filtered gradient² which does not correspond to the gradient of the small-scale
336 solution. This distinction disappears in the original formulation employing a convolution filter.

337 Other variants of the VMS model have been proposed in the literature. They include the
338 *large-small* [16] and the *all-small* [25] approaches which correspond to evaluating the eddy vis-
339 cosity from either the low-pass filtered gradients or all the resolved scales.

340 Vreman [2] has proposed to discard the outer filter in Eq. (29) leading to

¹Other choices can be employed for the definition of the large-scale space. Further discussion on this topic is presented in Appendix B.

²When employing the BR1 and BR2 schemes this requires the use of the filtered lifted derivatives (see e.g. [41]).

$$(\nabla \cdot \mathcal{F}_m(\bar{\mathbf{u}}_h))_{\text{Vrem}} = \nabla \cdot (2\nu_s(\mathbb{P}_{V^s}[\nabla \bar{\mathbf{u}}_h])S(\mathbb{P}_{V^s}[\nabla \bar{\mathbf{u}}_h])) \quad . \quad (30)$$

341 This approach has led to qualitatively similar results to the *small-small* approach [2]. However it
 342 is not consistent with the original formulation by Hughes et al. [16] and is more closely related to
 343 the high-pass filtered Smagorinsky model [42]. This formulation has nonetheless the advantage
 344 of reducing the number of filtering operations required for the evaluation of the model. A large
 345 reduction of its computational cost can therefore be obtained for some formulations of the DG
 346 method (e.g. nodal DG).

347 Chapelier et al. [3] have proposed an *all-all* approach consisting in retaining only the outer
 348 filtering operation

$$(\nabla \cdot \mathcal{F}_m(\bar{\mathbf{u}}_h))_{\text{a-a}} = \mathbb{P}_{V^s} [\nabla \cdot (2\nu_s(\nabla \bar{\mathbf{u}}_h)S(\nabla \bar{\mathbf{u}}_h))] \quad . \quad (31)$$

349 This approach is specifically tailored for the DG-modal formulation employing orthonormal
 350 hierarchical bases. In this case the outer filtering operation can be implicitly applied by removing
 351 the model term from the equation of the modal coefficients associated with the large-scale space
 352 basis functions. Thus the *all-all* approach presents the same computational cost as the standard
 353 Smagorinsky model for this class of methods.

354 In Sec. 6 the three variants of the DG-VMS approach here described are compared by analysing
 355 their accuracy in replicating the ideal energy transfer mechanism.

356 5. Ideal energy transfer from DNS data

357 The methodology laid out in the Sec. 3 is applied to three DNS data sets of the TGV con-
 358 figuration at $\text{Re} = 5\,000$, $20\,000$ and $40\,000$. The reference DNS have been performed using the
 359 sixth-order incompressible flow solver *Incompact3D* [24]. The considered computations have
 360 been obtained on a regular Cartesian mesh of respectively 1280^3 , 3456^3 and 5400^3 nodes in a
 361 triperiodic domain of $[-\pi, \pi]^3$ using symmetries to divide by 8 the number of degrees of free-
 362 dom (dofs) actually computed. A snapshot of each of these data sets at $t = 14$ (non-dimensional
 363 time units) is selected for analysis. At this time the flow is fully developed in a state close to
 364 isotropic and homogeneous conditions with values of the Reynolds number based on the Taylor
 365 microscale $\text{Re}_\lambda = 136$, 286 and 400 for $\text{Re} = 5\,000$, $20\,000$ and $40\,000$ respectively.

366 In Fig. 1 we report the energy spectrum of the snapshot corresponding to $\text{Re} = 5\,000$. On the
 367 same figure we report the energy spectra of the ideal DG-LES solution for $p = 7$ and respectively
 368 72^3 , 144^3 and 288^3 dofs, computed as described in Appendix A.

369 When analysing DG-LES simulation results it is assumed that the resolution limit is defined
 370 by the cut-off frequency $k_{\text{DG}} = \frac{\pi(p+1)}{h} = \frac{(p+1)n_{el}}{2}$ (marked by black dashed lines in Fig. 1) where
 371 n_{el} is the number of elements in one direction. By analysing Fig. 1, however, it can be observed
 372 that the DG-LES spectrum is almost undistinguishable from that corresponding to the DNS up to
 373 a frequency $\tilde{k}_{\text{DG}} = \frac{(p+1)n_{el}}{3}$ and decays rapidly for higher frequencies. Moreover, the energy spec-
 374 trum is ‘‘polluted’’ by the presence of discontinuities for frequencies close to k_{DG} . Additionally
 375 the discontinuities generate a tail on the energy spectrum that decays as k^{-2} . It is argued therefore
 376 that \tilde{k}_{DG} is more relevant in identifying the resolving capabilities of the DG discretization. We
 377 will see in Sec. 5.2 that these observations are valid for other values of the polynomial degree p .

378 The values of \tilde{k}_{DG} for the three discretizations considered are therefore also reported in Fig. 1.
 379 These frequencies fall respectively within the inertial range ($E \propto k^{-5/3}$), at the end of the inertial
 380 range and in the dissipation range.

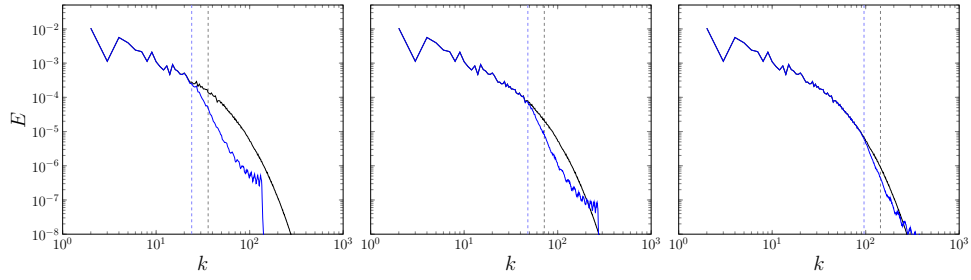


Figure 1: TGV at $Re = 5000$: Energy spectra from the DNS computation (black) and the ideal DG-LES solution (blue) for various discretizations: $p = 7$ and 72^3 , 144^3 and 288^3 dofs. Dashed lines indicate the corresponding value of k_{DG} (black) and \bar{k}_{DG} (blue).

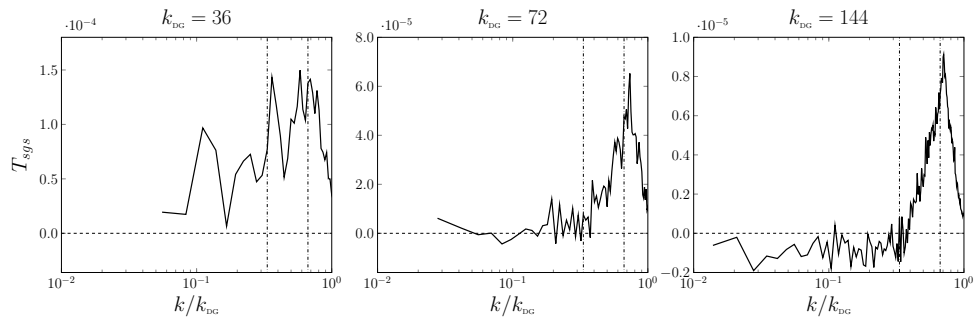


Figure 2: TGV at $Re = 5000$: Ideal SGS dissipation spectrum for three discretizations with $p = 7$. The values \bar{k}_{DG} and $\bar{k}_{DG}/2$ are marked by dash-dotted lines.

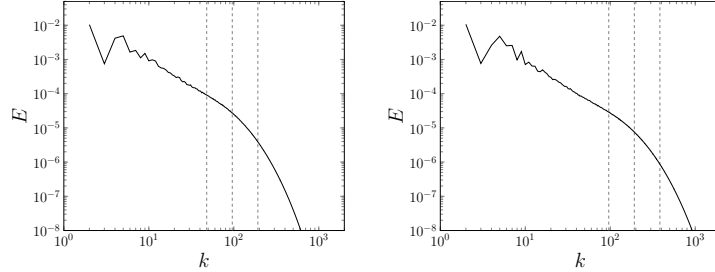


Figure 3: Energy spectra and relevant values of \tilde{k}_{DG} for the TGV at Re = 20 000 (left), 40 000 (right).

381 In Fig. 2 we report the ideal SGS dissipation spectra, as defined in Eq. (15), computed for the
 382 three considered resolutions. In each plot, we observe that the dissipation spectrum presents a
 383 peak at \tilde{k}_{DG} and rapidly decays for higher frequencies. This behaviour is remarkably different as
 384 compared to the case of sharp spectral filters for which a cusp appears at the cut-off frequency.
 385 This observation further confirms the relevance of \tilde{k}_{DG} in identifying the resolving capabilities of
 386 the employed discretization.

387 As regards the lower frequencies, we observe that for the coarsest employed discretization
 388 the interaction between the largest-resolved scales and the unresolved scales is non-negligible.
 389 As the value of \tilde{k}_{DG} is moved toward the dissipation range, we observe from the middle and right
 390 panel of Fig. 2 a clearly different behaviour. In this case the ideal energy transfer is negligible up
 391 to a frequency corresponding to $\tilde{k}_{\text{DG}}/2 = k_{\text{DG}}/3$ and the dissipation spectrum rapidly increases up
 392 to \tilde{k}_{DG} corresponding to a hyperviscous-type behaviour. A sharper peak of the SGS dissipation
 393 spectrum is observed as the resolution is increased. Additionally for the finest resolution consid-
 394 ered $k_{\text{DG}} = 144$ the ideal energy transfer is negative for frequencies below $k_{\text{DG}}/3$ corresponding
 395 to backscatter. While similar results are seldom presented in the literature we mention that both
 396 Domaradzki [9] and Métais and Lesieur [11] reported negative values of the eddy viscosity in the
 397 smallest wavenumber range employing an isotropic sharp spectral filter with cut-off frequency
 398 in the dissipation range. Moreover Métais and Lesieur [11] have shown that with this type of
 399 LES filter a negative value of the plateau of the eddy viscosity is obtained assuming an energy
 400 spectrum $E(k) \propto k^{-m}$ with $m \geq 5$.

401 In order to analyse the generality of these observations we consider now the TGV configu-
 402 ration at higher Reynolds numbers, namely Re = 20 000 and 40 000. The corresponding energy
 403 spectra are reported in Fig. 3 as well as the values of \tilde{k}_{DG} corresponding to three discretizations
 404 considered. These discretizations correspond to $p = 7$ and a number of dofs equal to 144^3 , 288^3
 405 and 576^3 for the lower Reynolds number and 288^3 , 576^3 and 1152^3 for the higher Reynolds
 406 number configuration. For both configurations the coarsest discretizations correspond to \tilde{k}_{DG}
 407 in the inertial range, whereas the finer discretizations correspond respectively to \tilde{k}_{DG} at the end of
 408 the inertial range and \tilde{k}_{DG} in the dissipation range.

409 For both configurations and all resolutions considered we observe in Figs. 4 and 5 again a
 410 peak of the dissipation spectrum at \tilde{k}_{DG} and a rapid decay towards k_{DG} , confirming the results
 411 obtained for the configuration at Re = 5 000. In this case, however, for the two lower resolutions,
 412 with \tilde{k}_{DG} located in the inertial range, we observe a mixed viscous-hyperviscous behaviour. The
 413 viscous type behaviour, corresponding to an ideal SGS dissipation spectrum which scales as $k^{\frac{1}{3}}$,
 414 is dominant for the low and intermediate wavenumbers up to approximately $k_{\text{DG}}/3$ whereas the

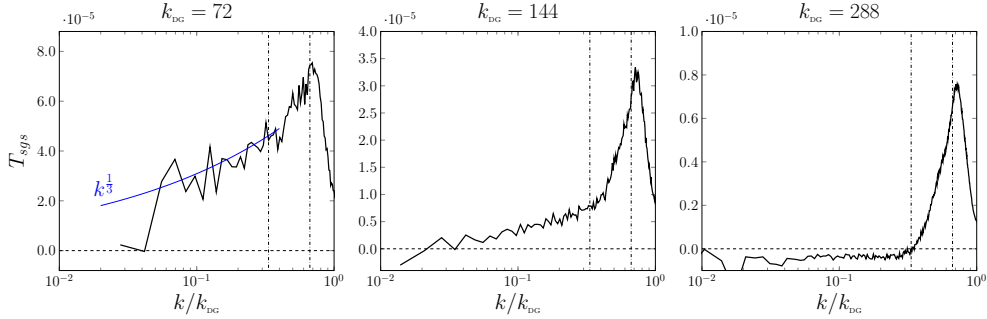


Figure 4: TGV at $Re = 20\,000$: Ideal SGS dissipation spectrum for three discretizations with $p = 7$. The values \tilde{k}_{DG} and $\tilde{k}_{DG}/2$ are marked by dash-dotted lines.

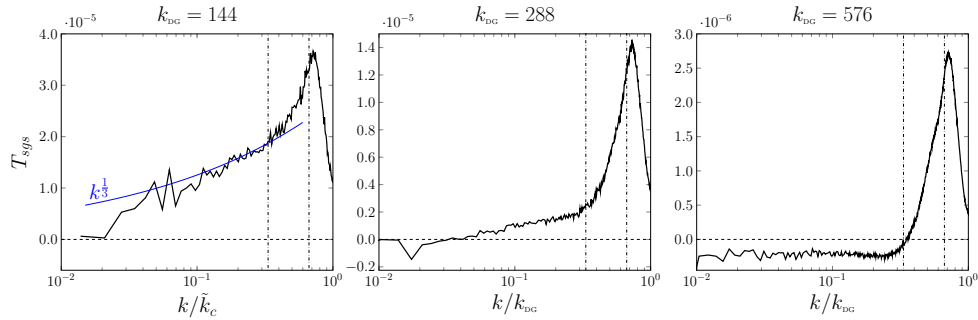


Figure 5: TGV at $Re = 40\,000$: Ideal SGS dissipation spectrum for three discretizations with $p = 7$. The values \tilde{k}_{DG} and $\tilde{k}_{DG}/2$ are marked by dash-dotted lines.

415 hyperviscous behaviour is dominant for higher frequencies up to \tilde{k}_{DG} .

416 However, as resolution is increased, the contribution of wavenumbers below $k_{DG}/3$ to the total
 417 SGS dissipation is progressively reduced and most of the SGS dissipation acts on the frequencies
 418 $[k_{DG}/3, k_{DG}]$. Eventually, as the resolution is further increased and \tilde{k}_{DG} moves into the dissipation
 419 range, the interaction between the large-resolved scales and unresolved scales becomes negligi-
 420 ble. This can be observed in the right panels of Figs. 4 and 5. In this case, the energy transfer
 421 is dominated by the SGS dissipation acting on frequencies $[k_{DG}/3, k_{DG}]$. For frequencies below
 422 $k_{DG}/3$ the energy transfer is predominantly negative corresponding to backscatter.

423 The results obtained therefore indicate that the large-resolved scales are free of interaction
 424 with the unresolved ones only when the DG-LES limit of resolution falls at the end of the inertial
 425 range and within the dissipation range. When a coarser resolution is employed, a mixed
 426 viscous-hyperviscous type behaviour can be observed and the SGS dissipation acting on the
 427 large-resolved scales is not negligible.

428 The mixed type behaviour is not observed in Fig. 2 as the TGV at $Re = 5\,000$ presents a very
 429 short inertial range.

430 5.1. Ideal modal energy transfer and eddy viscosity

431 We now analyse the modal energy transfer as defined by Eq. (20) for the same configurations
 432 described in the previous section. Obtained results are reported in Fig. 6. We observe a remark-

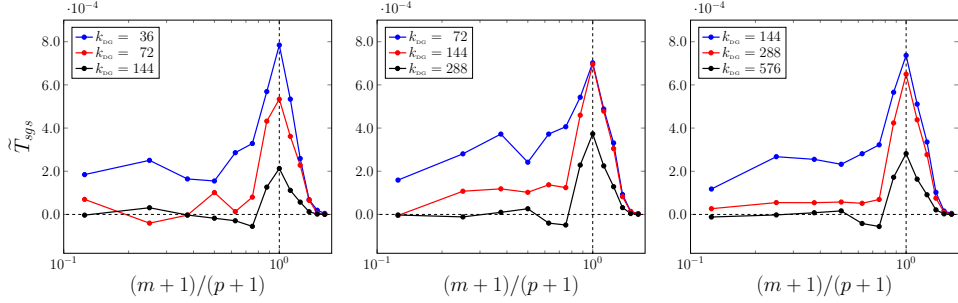


Figure 6: Modal energy transfer for the ideal SGS stress for the TGV at $Re = 5000$ (left), 20000 (center), and 40000 (right) for various discretizations with $p = 7$.

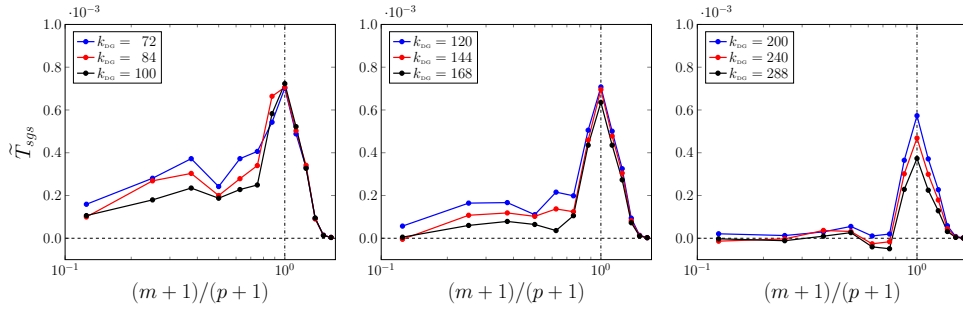


Figure 7: TGV at $Re = 20000$: Modal energy transfer for the ideal SGS stress for several discretizations with $p = 7$.

ably consistent behaviour across all resolutions and Reynolds numbers considered. A first region can be identified which is characterized by a nearly constant modal energy transfer for mode-numbers m from 0 to 5. The modal energy transfer then increases rapidly presenting a peak at $m = p$ and then decreases smoothly for higher mode-numbers. We remark that these two different behaviours are separated by the same mode-number corresponding to $(m + 1)/(p + 1) = 0.75$ for all the discretizations and Reynolds numbers considered.

As we would expect from the previous analysis in Fourier space, the energy transferred to modes corresponding to low mode-numbers is not in general negligible. As the discretization is refined this value progressively decreases and the energy transfer mechanism is dominated by the SGS dissipation acting on modes $(m + 1)/(p + 1) > 0.75$.

To further verify that this result is not specific to the chosen resolutions, we report in Fig. 7 the modal energy transfer obtained at $Re = 20000$ for 9 discretizations with $p = 7$ and a number of dofs between 144^3 and 576^3 . This figure clearly illustrates the consistency of the described behaviour. We further observe that for relatively coarse discretizations as the resolution is increased, the main effect is to reduce the modal energy transfer at low mode-numbers. Only when the resolution limit is in the dissipation range ($k_{DG} > 168$) we observe a significant reduction of the peak value as the discretization is further refined.

The ideal modal eddy viscosity, as defined in Eq. (22) using the BR1 scheme for the viscous discretization, is reported in Fig. 8 for the three Reynolds numbers and discretizations.

Similarly to what has been observed for the modal energy transfer, the modal eddy viscosity

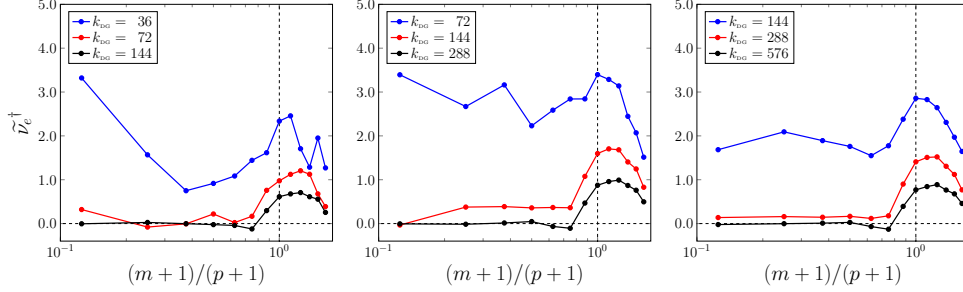


Figure 8: Ideal modal eddy viscosity for the ideal subgrid stress for the TGV at $Re = 5000$ (left), 20000 (center), 40000 (right) for various discretizations with $p = 7$.

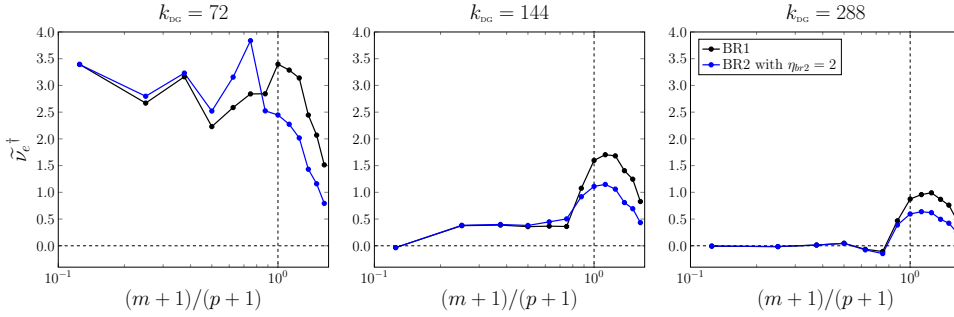


Figure 9: TGV at $Re = 20000$: Ideal modal eddy viscosity for the ideal SGS stress using the BR1 and BR2 schemes.

453 presents a plateau at mode-numbers $m \leq 5$ and increases for higher mode-numbers. In con-
 454 trast to the modal dissipation spectrum, however, the modal eddy viscosity presents in general
 455 a “parabolic” shape (in place of a spike) with a smoother increase and decay for relatively high
 456 mode-numbers.

457 We remark that the values reported in Fig. 8 correspond to the ideal modal eddy viscosity that
 458 should be provided by the SGS model employing the BR1 discretization. In Fig. 9 we compare
 459 this value with the modal eddy viscosity corresponding to the BR2 scheme with $\eta_{br2} = 2$.

460 As expected the additional dissipation provided by the BR2 scheme leads to a reduction
 461 of the modal eddy viscosity required at the higher mode-numbers. This result agrees with the
 462 observation that the optimal LES model must be aware of the discretization employed due to
 463 their interaction in actual simulations.

464 To conclude this analysis we observe that all the obtained results indicate that the interac-
 465 tion between large-resolved scales and unresolved ones, when employing the DG-LES filter, is
 466 negligible only for finite Reynolds numbers when the turbulent scales are resolved up to the end
 467 of the inertial range. Based on these findings, it could be argued that models based on this as-
 468 sumption present a limited applicability as they would rely on high resolution being available
 469 and thus provide a limited computational gain as compared to (underresolved) DNS. We want
 470 to remark however that the resolution requirements in an actual simulation vary in space and
 471 time and thus this assumption might be locally valid. This is the case for transitional or spatially
 472 inhomogeneous flows.

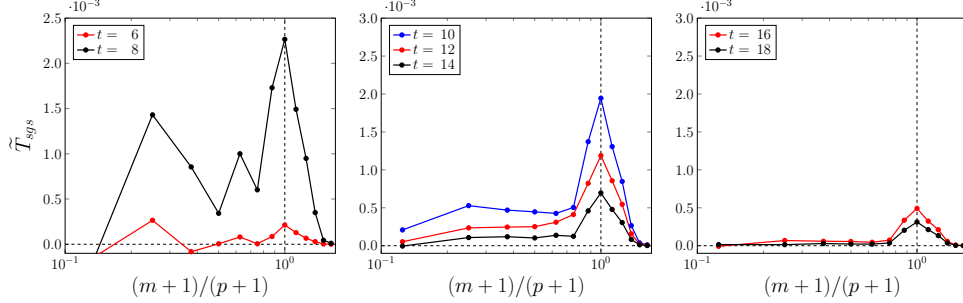


Figure 10: TGV at $Re = 20\,000$: Ideal modal energy transfer for the ideal SGS stress at various times for $p = 7$ and 288^3 dofs.

473 As an example, we illustrate in Fig. 10 the modal energy transfer for the TGV at $Re = 20\,000$
 474 at various times for a discretization corresponding the intermediate resolution considered ($p = 7$,
 475 $n_{el} = 36$ and 288^3 dofs). It can be observed that the SGS dissipation rapidly increases during
 476 the transition phase (left panel of Fig. 10) and the energy transfer from large scales remains
 477 non negligible during the first part of the decay phase (central panel). However for $t > 14$ the
 478 resolution is sufficient such that the energy transfer from modes $m \leq 5$ is clearly negligible
 479 (right panel). Thus the ideal LES model should be able to adapt to each of these conditions by
 480 reducing the SGS model dissipation applied to large scales during the initial transition phase and
 481 late dissipation phase.

482 5.2. Sensitivity to the polynomial degree

483 In this section we investigate the generality of the obtained results by analysing discretiza-
 484 tions corresponding to various values of the polynomial degree p . All the results here reported
 485 have been obtained from a snapshot at $t = 14$ of the TGV at $Re = 20\,000$. The comparisons are
 486 carried out by fixing the total number of dofs to the same values employed in Sec. 5, that is 144^3 ,
 487 288^3 and 576^3 dofs. Four values of the polynomial degree are at first considered: $p = 5, 7, 8$,
 488 and 11 .

489 Fig. 11 presents the energy spectra of the DNS data set and the ideal DG-LES solutions for
 490 all considered discretizations. We observe that for a fixed number of dofs the energy spectra are
 491 almost identical up to k_{DG} and as mentioned in the previous section (see Fig. 1) identical to the
 492 DNS spectrum up to \tilde{k}_{DG} . The most notable differences appear in the tail of the spectra related to
 493 the discontinuities of the DG-LES solutions. Thus we can reasonably conclude that increasing
 494 the polynomial degree for a fixed number of dofs has a limited effect on the resolving capabilities
 495 of the DG-LES method.³

496 This conclusion is also confirmed by analysing Fig. 12 which reports the SGS dissipation
 497 spectrum. Indeed the same behaviour can be observed for all polynomial degrees confirming the
 498 generality of the conclusions drawn in the previous section.

499 In Figs. 13 and 14 we report the modal energy transfer and eddy viscosity. The modal energy
 500 transfer levels cannot be directly compared, as a different number of modes is retained for each

³This observation only concerns the accuracy of the considered solution space in representing the DNS solution. It does not take into account the dissipation properties of the numerical fluxes as done e.g. by Moura et al. [43].

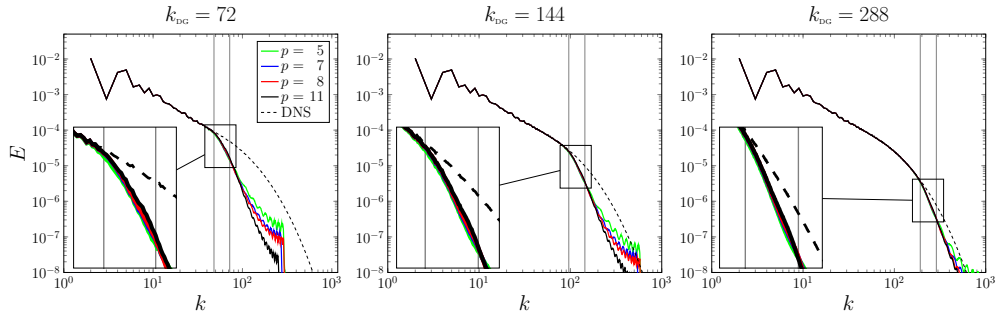


Figure 11: TGV at $Re = 20\,000$: Energy spectra of the DNS data and the ideal DG-LES solution for various discretizations for 144^3 , 288^3 and 576^3 dofs. Close-up view at frequencies between \bar{k}_{DG} and k_{DG} .

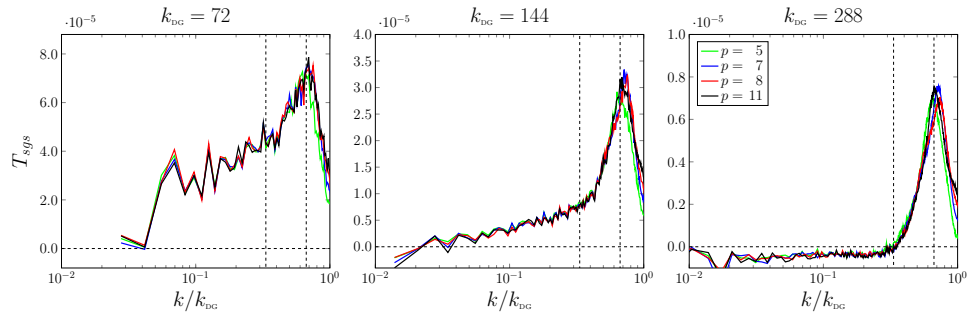


Figure 12: TGV at $Re = 20\,000$: Ideal SGS dissipation spectrum for various discretizations for 144^3 , 288^3 and 576^3 dofs. Dashed lines mark values of \bar{k}_{DG} and $\bar{k}_{DG}/2$.

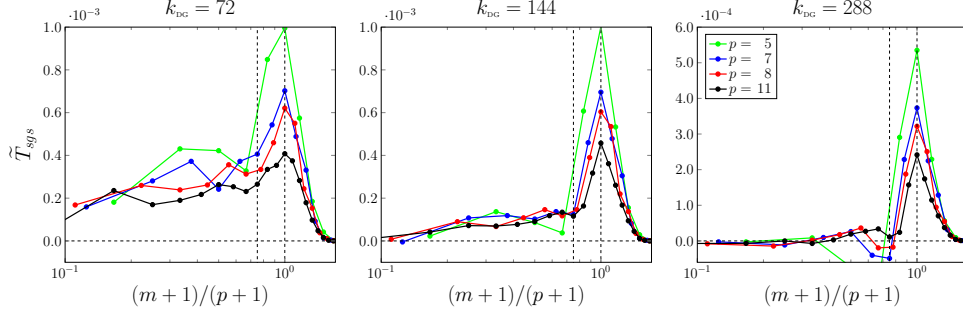


Figure 13: TGV at $\text{Re} = 20000$: Ideal modal energy transfer for various discretizations for 144^3 , 288^3 and 576^3 dofs. Dashed lines indicate mode-numbers $m + 1 = 0.75(p + 1)$ and $m = p$.

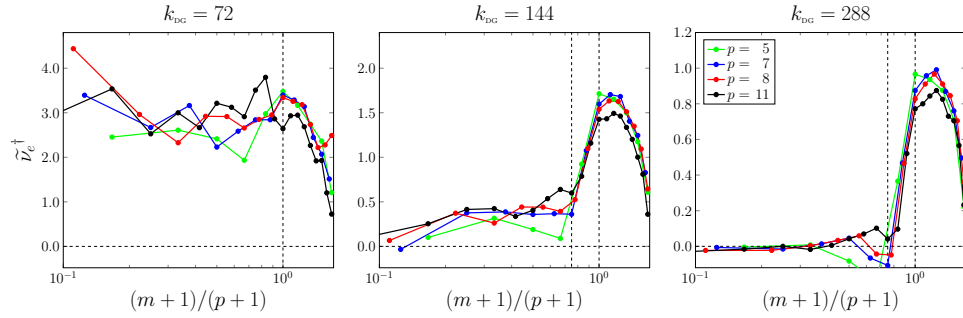


Figure 14: TGV at $\text{Re} = 20000$: Ideal modal eddy viscosity for various discretizations for 144^3 , 288^3 and 576^3 dofs. Dashed lines indicate mode-numbers $m + 1 = 0.75(p + 1)$ and $m = p$.

501 polynomial degree, however we can observe that the same trend seen for $p = 7$ (see Sec. 5.1) is
 502 obtained for the other discretizations. In particular, we remark the presence of nearly constant
 503 value for mode-numbers up to approximately $m + 1 = 0.75(p + 1)$ and a peak at $m = p$ for the
 504 modal energy transfer. The generality of our conclusions is further illustrated by Fig. 14 which
 505 demonstrates the close agreement of the modal eddy viscosity for all discretizations and confirms
 506 the relevance of the mode-number $m + 1 = 0.75(p + 1)$ in separating the two different behaviours.

507 We consider now relatively lower polynomial degree representations: $p = 2, 3, 4$ and 5 . The
 508 energy spectra for all discretizations are not reported here as they lead to the same conclusions
 509 drawn from Fig. 11. More marked differences can be observed in Figs. 15 and 16 reporting
 510 the ideal SGS dissipation spectrum and modal eddy viscosity. Overall a similar behaviour can
 511 be recognized for different values of p in Fig. 15. As observed for relatively higher values of
 512 p , as the resolution is increased the SGS dissipation concentrates on the scales characterized
 513 by higher wavenumbers, and eventually the SGS dissipation acting on wavenumbers lower than
 514 $k_{\text{DG}}/3$ becomes negligible. In contrast with the results obtained for higher polynomial degrees,
 515 the presence, location and value of the peak of the SGS dissipation spectrum appear to be dependent
 516 on the polynomial degree for $p \leq 4$.

517 Similarly, in Fig. 16 we observe relatively marked differences in the modal eddy viscosity
 518 for different values of p . As the resolution is increased the SGS dissipation acts on the highest

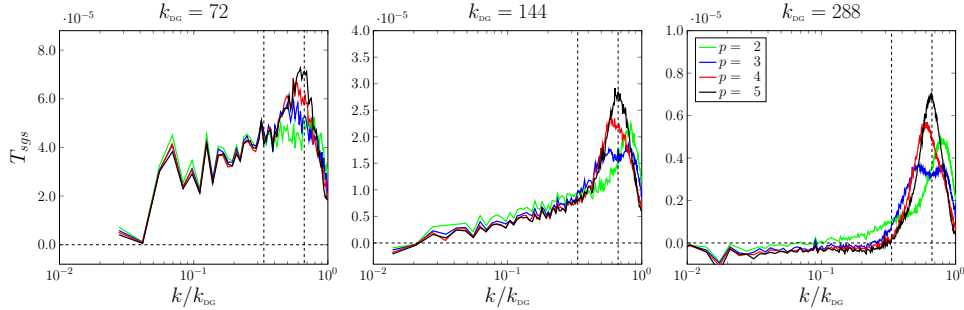


Figure 15: TGV at $\text{Re} = 20\,000$: Ideal SGS dissipation spectrum for various discretizations for 144^3 , 288^3 and 576^3 dofs. Dashed lines mark values of \tilde{k}_{DG} and $\tilde{k}_{\text{DG}}/2$.

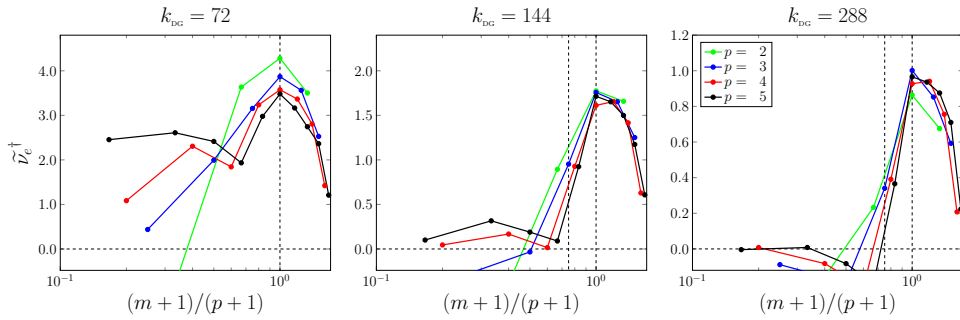


Figure 16: TGV at $\text{Re} = 20\,000$: Ideal modal eddy viscosity for various discretizations for 144^3 , 288^3 and 576^3 dofs. Dashed lines indicate mode-numbers $m + 1 = 0.75(p + 1)$ and $m = p$.

519 modenumbers. However compared to Fig. 14, no real plateau can be identified for the modal
 520 eddy viscosity at low modenumbers. For the highest resolution (right panel of Fig. 16) relatively
 521 higher values of the modal eddy viscosity are obtained for $m + 1 \geq 0.75(p + 1)$, similarly to what
 522 observed for $p \geq 5$, however, markedly negative values are obtained for the modal viscosity at
 523 low modenumbers.

524 5.3. Effect of the DG-LES filter

525 As discussed in Sec. 2, all the results presented have been obtained by defining the ideal
 526 DG-LES solution as the L^2 -projection on the discretization space of the DNS solution filtered
 527 with a sharp spectral filter removing frequencies $\|\mathbf{k}\|_\infty \geq k_{\text{DG}}$. Other possible definitions can be
 528 considered. Among them, the L^2 -projection of the DNS solution on the DG discretization space
 529 is an interesting candidate.

530 The effect of these two different definitions on the results obtained is therefore investigated.
 531 For this purpose we employ the snapshot at $t = 14$ of the TGV at $\text{Re} = 20\,000$. In order to
 532 simplify the notation we will refer to the L^2 -projection of the DNS solution on the DG space as
 533 simply the DG-projection in contrast to the employed definition of ideal DG-LES solution.

534 In Fig. 17 we report the energy spectra corresponding to the ideal DG-LES and the DG-projection
 535 for three resolutions. We observe that for all resolutions the energy spectra are indistinguishable
 536 for frequencies up to \tilde{k}_{DG} . Moreover we notice remarkably higher values of the tail of the energy

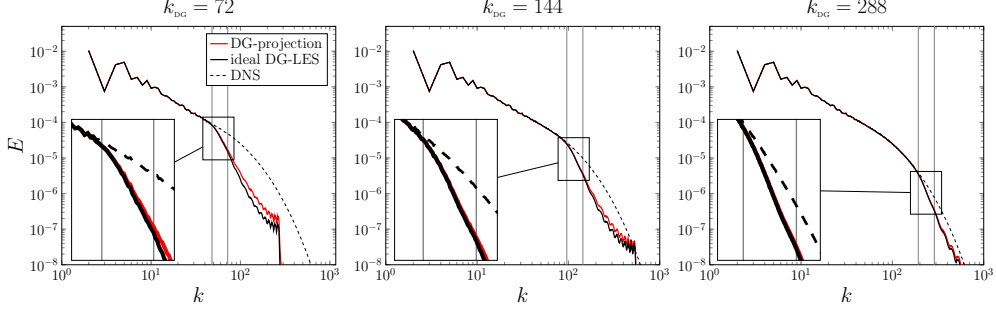


Figure 17: TGV at $Re = 20000$: Energy spectra of the DNS data, the ideal DG-LES solution, and DG-projection for three resolutions with $p = 7$. Close-up view for frequencies between \tilde{k}_{DG} and k_{DG} .

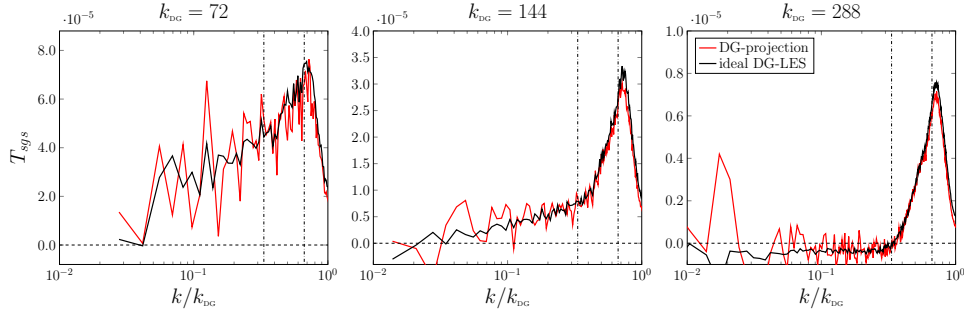


Figure 18: TGV at $Re = 20000$: Ideal SGS dissipation spectrum of the ideal DG-LES solution and the DG-projection for three discretizations with $p = 7$. Dashed lines mark values of \tilde{k}_{DG} and $\tilde{k}_{DG}/2$.

537 spectra for the DG-projection which is especially evident in the coarsest resolution (left panel of
 538 Fig. 17). This indicates, as one would expect, that the L^2 -projection of the DNS field presents
 539 stronger discontinuities than the L^2 -projection of the filtered field. Nonetheless, \tilde{k}_{DG} appears to
 540 be a relevant frequency identifying the resolution properties of DG using both definitions.

541 In Fig. 18 and 19 we present the spectral and modal energy transfer for the same resolutions.
 542 These figures illustrate a fair agreement between results obtained with the two definitions. The
 543 most remarkable differences appear in Fig. 18 for the relatively low frequencies. Indeed the
 544 DG-projection leads to a more erratic behaviour of the spectral energy transfer which could be
 545 explained by the presence of aliasing errors as described in Sec. 2.

546 Slightly more significant differences can be observed in Fig. 20 which reports the modal
 547 eddy viscosity employing the BR1 scheme. In this figure we can identify lower values of the
 548 modal eddy viscosity at relatively high mode-numbers. These can be explained by the presence
 549 of stronger discontinuities and higher values of the lifting coefficients used for the BR1 scheme
 550 and therefore, higher values of the diffusive term in the denominator of Eq. (22) at high mode-
 551 numbers.

552 Overall the results obtained demonstrate that, with the exception of small differences, the
 553 definition of the reference DG-LES solution as the L^2 -projection of the DNS field leads to the
 554 same conclusions drawn by employing the current definition of the ideal DG-LES solution.

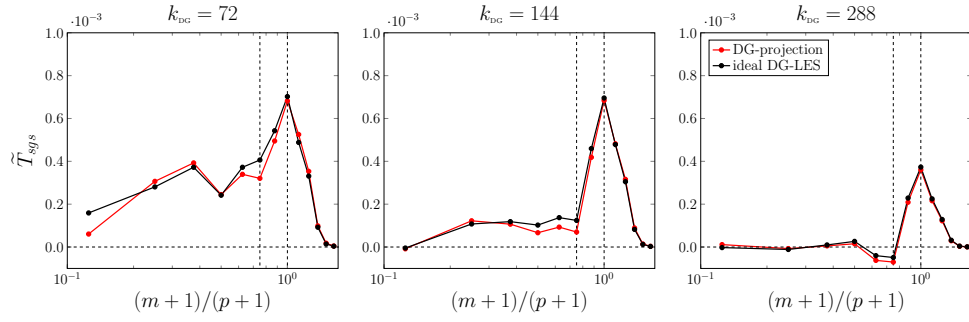


Figure 19: TGV at $Re = 20000$: Ideal modal energy transfer of the ideal DG-LES solution and the DG-projection for three discretizations with $p = 7$. Dashed lines indicate mode-numbers $m + 1 = 0.75(p + 1)$ and $m = p$.

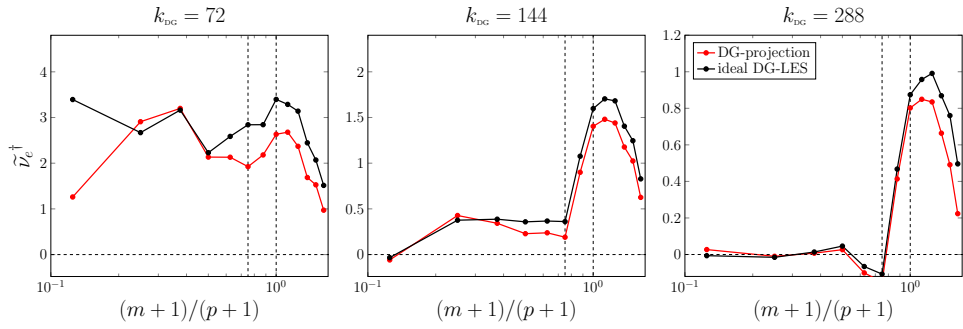


Figure 20: TGV at $Re = 20000$: Ideal modal eddy viscosity of the ideal DG-LES solution and the DG-projection for three discretizations with $p = 7$. Dashed lines indicate mode-numbers $m + 1 = 0.75(p + 1)$ and $m = p$.

555 **6. A-priori analysis of the DG-VMS approach**

556 In this section, we perform an *a-priori* analysis of the DG-VMS model based on the three
 557 variants described in Sec. 4. For this purpose, we evaluate the DG-VMS model from the ideal
 558 DG-LES solution corresponding to $Re = 20\,000$ and $t = 14$ for $p = 7$ and $n_{el} = 72$. As described
 559 in the previous section, for this Reynolds number and discretization considered the resolution
 560 limit, $\tilde{k}_{DG} = 192$, falls within the dissipation range. Under these conditions the interaction be-
 561 tween large-resolved and unresolved scales is negligible (see Fig. 4) and we expect the DG-VMS
 562 approach to recover the ideal SGS dissipation.

563 The three variants of the DG-VMS model are therefore evaluated from this solution for dif-
 564 ferent values of the scale fraction parameter β . For all three variants we do not consider the
 565 calibration of the model coefficients, as described e.g. by Meyers et al. [44], as a function of β .
 566 One reason for not employing such calibration is that it is derived for convolution filters. As we
 567 have observed in Sec. 2, this is not the case for the DG-projection and additional care is required
 568 to derive a consistent calibration procedure. Additionally it has been shown by Meyers et al. [44]
 569 that the model constant is dependent on the ratio Δ/η , where η is the Kolmogorov scale, when
 570 $\Delta/\eta \leq 100$. This is the case when the DG-LES resolution falls at the beginning of the dissipation
 571 range as considered here. Thus we also make no attempt at providing a general calibration of the
 572 model coefficient from the employed DNS/LES data as the results would be dependent on this
 573 parameter in the range of validity of the DG-VMS approach. In order to facilitate the analysis,
 574 all the results are presented with the model constant selected such that the modelled dissipation
 575 spectrum presents the same maximum value as that of the ideal SGS dissipation spectrum. The
 576 employed values of the model coefficient are reported in Table 1.

	BR1			BR2 $\eta_{br2} = 2$		
	$\beta = 0.25$	$\beta = 0.5$	$\beta = 0.75$	$\beta = 0.25$	$\beta = 0.5$	$\beta = 0.75$
all-all	0.093	0.103	0.122	0.094	0.096	0.098
Vreman	0.099	0.120	0.181	0.099	0.117	0.162
small-small	0.102	0.122	0.156	0.103	0.112	0.139
Smagorinsky	0.090			0.090		

Table 1: TGV at $Re = 20\,000$, $p = 7$, $k_{DG} = 288$: Model coefficients selected for the Smagorinsky and DG-VMS model using the BR1 and BR2 schemes.

577 In Fig. 21 we report the ideal and model SGS dissipation spectrum corresponding to the
 578 Smagorinsky model and the three variants of the DG-VMS approach using the BR1 discretization
 579 scheme.

580 It is obvious from this figure that, as already shown by other authors, the Smagorinsky model
 581 provides excessive dissipation at low wavenumbers. This effect is drastically reduced by em-
 582 ploying all the considered variants of the DG-VMS approach. As expected, increasing the value
 583 of β restricts the action of the SGS model on progressively finer scales and, for a fixed model
 584 constant, reduces the total SGS dissipation.

585 In particular for $\beta = 0.75$ the SGS model acts only on the range of scales $[k_{DG}/3, k_{DG}]$. For
 586 lower values of β however the distribution of the modelled SGS dissipation does not correspond
 587 to the ideal SGS dissipation for any of the considered discretizations. This effect is particu-

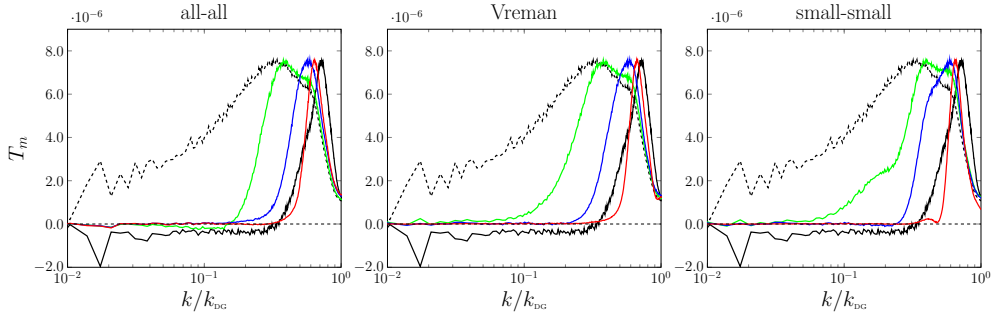


Figure 21: TGV at $\text{Re} = 20000$, $p = 7$, $k_{\text{DG}} = 288$: Ideal SGS energy transfer (black solid), SGS model dissipation spectrum provided by the Smagorinsky model (dashed) and three variants of the DG-VMS approach for: $\beta = 0.25$ (green), $\beta = 0.5$ (blue), and $\beta = 0.75$ (red) using the BR1 scheme.

larly marked for $\beta < 0.5$ and has also been observed by employing the DG-LES solution at the intermediate resolution $k_{\text{DG}} = 144$ (not reported here).

We further remark that the SGS dissipation spectrum decays smoothly for low wavenumbers for all variants of the DG-VMS approach. This is expected as the high-pass projection filter is not sharp in Fourier space. As Sagaut and Levasseur [27] have shown that a smooth decay of the SGS dissipation spectrum leads to improved results in a-posteriori tests, this result demonstrates an advantage of using a modal decomposition as opposed to an orthogonal spectral filter.

Among the three variants, the all-all approach presents the smoothest behaviour at low wavenumbers and the small-small approach presents the sharpest behaviour. Moreover we identify the presence of bumps in the SGS dissipation spectrum of the small-small variant, clearly visible for $\beta = 0.25$ in Fig. 21. These results indicate an advantage of the Vreman variant with respect to the small-small approach. Indeed we recall that the eddy viscosity and the strain rate are evaluated in the same way for the two variants and the obtained results show that removing the outer projection operation leads to a smoother SGS dissipation spectrum for a lower computational cost.

Comparing the all-all and the Vreman approaches is not as straightforward. Indeed we observe that the all-all variant presents a marginally better agreement with the ideal SGS dissipation spectrum and we recall that it presents a much lower computational cost for modal DG methods. However, in contrast to the all-all variant, for the Vreman approach the SGS model is computed from the filtered gradients. For this reason the SGS stress is aligned with the small-scale gradients and tends to zero when the flow is well resolved and the solution is represented entirely by the large-scale component. An analysis of the alignment between the ideal SGS stress and the modelled one could therefore be employed in order to draw more definitive conclusions.

Further analysing Fig. 21 we observe that, despite presenting a smooth decrease of the dissipation spectrum towards the low wavenumbers, all VMS approaches present a negligible amount of SGS dissipation acting on the large resolved scales. This confirms that the DG-VMS approach is not able to replicate the viscous-type behaviour observed at low wavenumbers when the resolution limit falls within the inertial range. Additionally we observe that the modelled energy transfer presents a small region with negative values for the all-all approach with $\beta = 0.25$. A similar result has been observed also for the small-small variant for other resolutions when low values of β are considered (not shown here). This effect has not been observed for the Vreman variant and is thus possibly caused by the outer high-pass L^2 -projection filter. These regions of

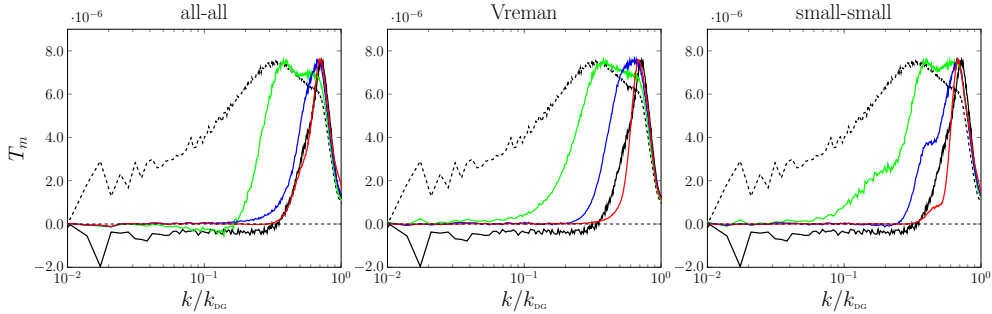


Figure 22: TGV at $Re = 20\,000$, $p = 7$, $k_{DG} = 288$: Ideal SGS energy transfer (black solid), SGS model dissipation spectrum provided by the Smagorinsky model (dashed) and three variants of the DG-VMS approach for: $\beta = 0.25$ (green), $\beta = 0.5$ (blue), and $\beta = 0.75$ (red) using the BR2 scheme ($\eta_{br2} = 2$).

620 negative energy transfer can therefore be considered as numerical artefact of the high-pass filter
 621 used in the DG-VMS approach and should not be interpreted as modelling backscatter.

622 Finally we note that for all VMS approaches with $\beta = 0.75$ the peak of the SGS dissipation
 623 spectrum is located at a relatively lower frequency compared to the ideal SGS dissipation spec-
 624 trum. This effect is partially explained by the use of the BR1 scheme in Fig. 21. Indeed, it is
 625 well known that the BR1 scheme presents very low and less than exact dissipation at frequencies
 626 close to k_{DG} [45]. A possible remedy is therefore to employ a different discretization for the SGS
 627 model term, e.g. the BR2 method.

628 In Fig. 22 we compare the ideal SGS dissipation spectrum and modelled energy transfer
 629 obtained with the BR2 scheme for $\eta_{br2} = 2$. As expected the presence of the penalty term in the
 630 BR2 scheme leads to a shift and increase of the model dissipation toward higher wavenumbers.
 631 However we remark that the optimal value of η_{br2} has been observed to depend on the employed
 632 discretization. Additionally for sufficiently high values of η_{br2} the dissipation provided by the
 633 SGS model might be overwhelmed by that introduced by the penalty term. A similar effect could
 634 be provided by the upwind dissipation associated to the discretization of the convective flux.

635 The conclusions drawn above are confirmed by analysing the modal energy transfer and eddy
 636 viscosity corresponding to the configuration considered in this section and the two discretization
 637 schemes BR1 and BR2. These are presented from Figs. 23 to 26.

638 It is clear from these figures that for the all-all approach a value of $\beta = 0.75$ must be employed
 639 in order to mimic the negligible ideal energy transfer at low mode-numbers. Additionally we
 640 observe that when employing the BR2 scheme with $\eta_{br2} = 2$ a remarkably good agreement
 641 is obtained with both the modal energy transfer and eddy viscosity, confirming the conclusion
 642 drawn from the spectral energy transfer analysis.

643 Considering now the Vreman and small-small approaches we observe that the outer filter
 644 operation does not appear necessary to limit the effect of the modelled dissipation on the highest-
 645 order modes. However we observe that while for the small-small variant $\tilde{T}_m = 0$ for $(m + 1)/(p +$
 646 $1) = \beta$, in the case of the Vreman approach it is positive and becomes negative for lower values
 647 of m . The combination of this positive and negative contribution leads to the smooth distribution
 648 of the modelled dissipation spectrum in Fig. 21 and 22.

649 In order to assess the generality of our remarks, we have repeated the presented analysis for
 650 different values of the polynomial degree p . Similar conclusions have been obtained with regards

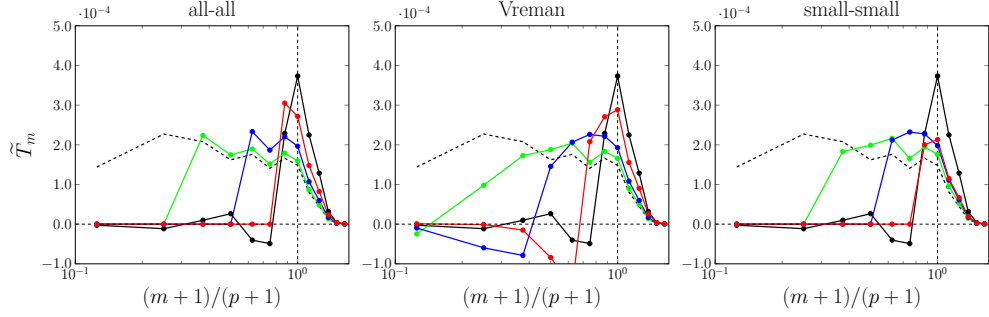


Figure 23: TGV at $Re = 20\,000$, $p = 7$, $k_{DG} = 288$: Ideal modal energy transfer (black solid) and modelled modal energy transfer provided by the Smagorinsky model (dashed) and three variants of the DG-VMS approach for: $\beta = 0.25$ (green), $\beta = 0.5$ (blue), and $\beta = 0.75$ (red) using the BR1 scheme.

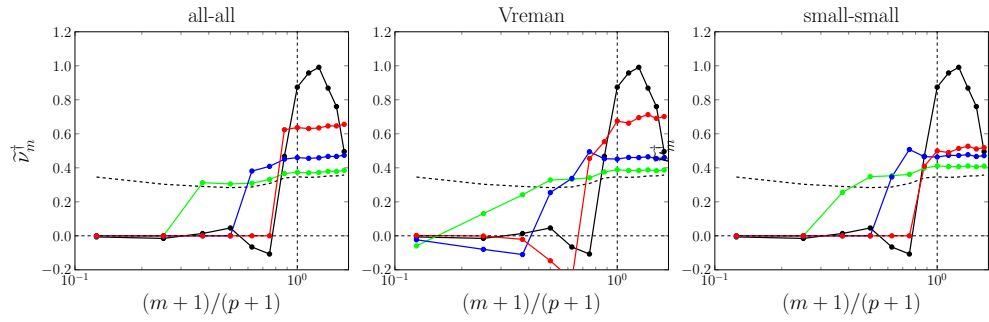


Figure 24: TGV at $Re = 20\,000$, $p = 7$, $k_{DG} = 288$: Ideal modal eddy viscosity (black solid) and modelled modal eddy viscosity provided by the Smagorinsky model (dashed) and three variants of the DG-VMS approach for: $\beta = 0.25$ (green), $\beta = 0.5$ (blue), and $\beta = 0.75$ (red) using the BR1 scheme.

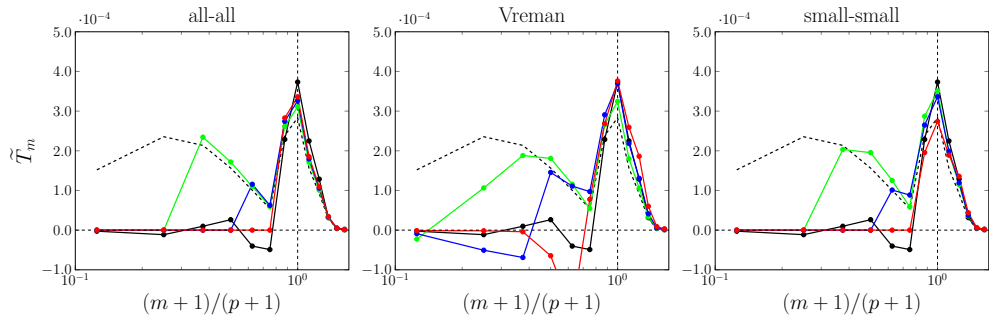


Figure 25: TGV at $Re = 20\,000$, $p = 7$, $k_{DG} = 288$: Ideal modal energy transfer (black solid) and modelled modal energy transfer provided by the Smagorinsky model (dashed) and three variants of the DG-VMS approach for: $\beta = 0.25$ (green), $\beta = 0.5$ (blue), and $\beta = 0.75$ (red) using the BR2 scheme ($\eta_{br2} = 2$).

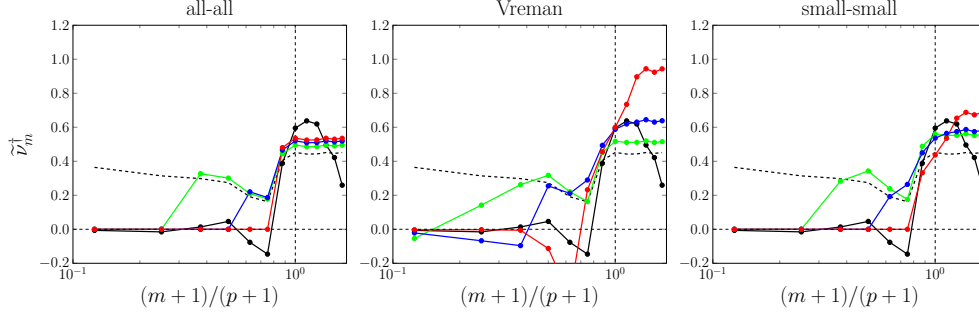


Figure 26: TGV at $Re = 20\,000$, $p = 7$, $k_{DG} = 288$: Ideal modal eddy viscosity (black solid) and modelled modal eddy viscosity provided by the Smagorinsky model (dashed) and three variants of the DG-VMS approach for: $\beta = 0.25$ (green), $\beta = 0.5$ (blue), and $\beta = 0.75$ (red) using the BR2 scheme ($\eta_{br2} = 2$).

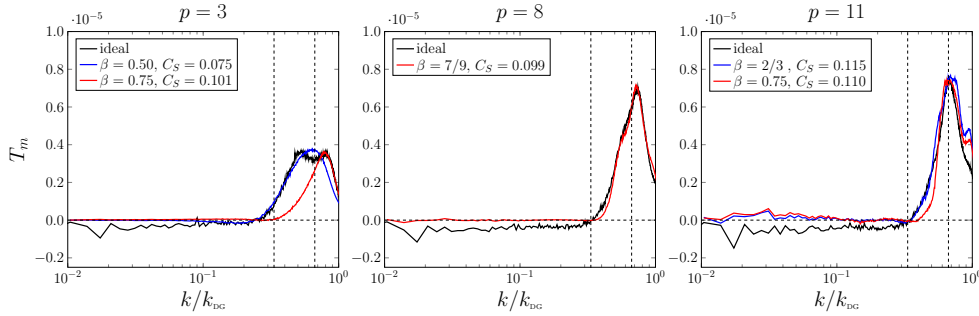


Figure 27: TGV $Re = 20\,000$: ideal SGS dissipation spectrum and model dissipation spectrum using the all-all DG-VMS approach with $C_S = 0.1$ using the BR2 scheme for $k_{DG} = 288$ and $p = 3$ (left), $p = 8$ (center) and $p = 11$ (right).

651 to the comparison of the three variants and the effect of variations of β on the model dissipation
 652 spectrum (not reported here). However, the optimal value of β appears to be dependent on p when
 653 $p \leq 4$. This result is expected from the *a-priori* analysis carried out in Sec. 5.2. To illustrate this,
 654 we report in Fig. 27 the ideal SGS dissipation spectrum and the model energy transfer for $p = 3$,
 655 8 and 11 using the DG-VMS all-all approach and the BR2 scheme ($\eta_{br2} = 2$).

656 We can observe that for $p = 8$ and 11 the value $\beta \approx 0.75$ leads to the modelled dissipation
 657 acting on the scales of wavenumbers in the range $[k_{DG}/3, k_{DG}]$ similarly to the ideal SGS dissi-
 658 pation spectrum. For $p = 3$, however, we observe that the ideal SGS dissipation spectrum does
 659 not present a peak at k_{DG} and the model dissipation presents a peak at a higher frequency. In this
 660 case the ideal SGS dissipation is in between that provided by the DG-VMS model for $\beta = 0.5$
 661 and $\beta = 0.75$. This result indicates that for $p \leq 4$ the DG-VMS approach might not be able to
 662 replicate the distribution of the ideal SGS dissipation.

663 The analysis presented up to this point has focused on the ability of the DG-VMS approach
 664 to replicate the ideal energy transfer mechanism when the resolution limit falls within the dissi-
 665 pation range and the SGS dissipation acting on large-resolved scales is negligible.

666 We have observed in Sec. 5 that when the resolution limit falls within the inertial range a
 667 viscous-type behaviour can be observed and is dominant at frequencies below $k_{DG}/3$. It appears
 668 from these analyses that the DG-VMS approach is not able to replicate this mechanism.

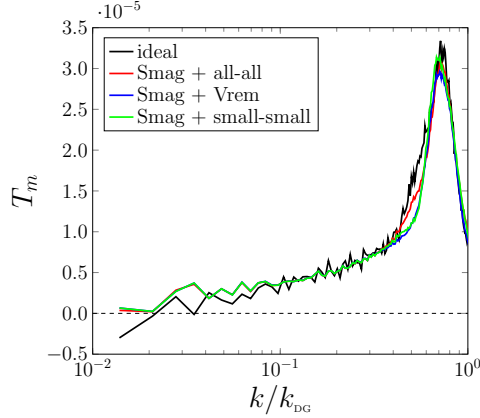


Figure 28: TGV $Re = 20\,000$, $p = 7$, $k_{DG} = 144$: Ideal SGS dissipation spectrum and modelled dissipation spectrum for mixed Smagorinsky+DG-VMS models.

669 Modifying or adapting β does not lead to a better representation of the SGS dissipation
 670 spectrum. However as we have observed in Fig. 21 this parameter allows to control the set
 671 of scales on which the SGS dissipation acts and the total amount of SGS dissipation. Thus
 672 the DG-VMS approach can nonetheless lead to improved results with respect to the standard
 673 or dynamic Smagorinsky model which might introduce in some cases excessive dissipation on
 674 the large resolved scales. This also explains the promising results observed for the local VMS
 675 approach proposed by Ramakrishnan and Collis [26] and for the dynamic partition selection al-
 676 gorithm for the DG-VMS approach by Naddei et al. [46].

677 The a-priori tests performed in this work indicate thus that the main limitation of the DG-VMS
 678 approach is its inability to mimic the energy transfer mechanism at low wavenumbers encoun-
 679 tered at high Reynolds and typical LES resolutions. This corresponds to a viscous-type be-
 680 haviour which can be modelled by an eddy-viscosity model such as the Smagorinsky model.
 681 The ideal SGS dissipation spectrum could be therefore approximated by employing a mixed
 682 Smagorinsky+DG-VMS model where the Smagorinsky model acts on all scales and the VMS ap-
 683 proach with $\beta = 0.75$ replicates the hyperviscous behaviour dominant on frequencies $k > k_{DG}/3$.
 684 The two model coefficients however should be dynamically adapted (e.g. using Germano's pro-
 685 cedure) as the relative contribution to the total SGS dissipation will depend on the resolution.

686 As an example, in Fig. 28 we consider the ideal SGS dissipation spectrum for a snapshot at
 687 $t = 14$ of the TGV at $Re = 20\,000$, $p = 7$ and 288^3 dofs. The ideal SGS dissipation spectrum is
 688 compared to the three variants of the mixed model with constant coefficients, for the Smagorin-
 689 sky contribution $C_{s,smag} = 0.057$ and $C_{s,a-a} = 0.063$ for the all-all variant, $C_{s,vrem} = 0.095$
 690 for the Vreman variant and $C_{s,s-s} = 0.087$ for the small-small variant. This figure illustrates
 691 that a dynamic mixed model even with global model coefficients has the potential to a very
 692 accurate agreement with the ideal SGS-dissipation. Similar approaches have already been pro-
 693 posed, e. g. the Smagorinsky and residual-based-VMS approach by Wang and Oberai [47], or
 694 the enhanced field model by Jeanmart and Winckelmans [13]. However this is the first work that
 695 demonstrates the potential of such methodology by *a-priori* analyses which include details of the
 696 numerical discretization and the effect of the DG-projection filter in the VMS approach.

697 **7. Conclusions**

698 In this work we have proposed a framework for the *a-priori* analysis of DG-LES methods
699 based on DNS databases. It is an extension of the classical framework for the analysis of the
700 energy transfer between resolved and unresolved scales of Kraichnan [8] and Domaradzki et
701 al. [9]. The proposed framework is consistent with the employed discretization and as such,
702 allows the evaluation of the ideal SGS dissipation spectrum that needs to be modelled including
703 the effect of discontinuities inherently present in the DG method and the particular choice of the
704 numerical flux.

705 We have further introduced the concept of a modal energy transfer and eddy viscosity. These
706 quantities can be employed to analyse *a-priori* LES models that rely on modifying the amount
707 of SGS dissipation acting on different modes of the solution such as the DG-VMS model and the
708 spectral vanishing viscosity approach.

709 The developed framework has been applied to a DNS database of the TGV at $Re = 5000$,
710 20000 and 40000 [24]. It has been shown that the ideal SGS dissipation spectrum presents in
711 general a mixed viscous-hyperviscous behaviour. The viscous behaviour is dominant for fre-
712 quencies below $k_{DG}/2 = k_{DG}/3 = n_{el}(p + 1)/6$ whereas the hyperviscous behaviour is dominant
713 at higher frequencies with a peak at k_{DG} . Only when the DG resolution limit falls at the begin-
714 ning of the dissipation range the energy transfer between large-resolved and unresolved scales
715 is negligible. This corresponds to a negligible energy transfer to DG modes of mode-number
716 $m + 1 \leq 0.75(p + 1)$. Under these conditions, the DG-VMS approach can provide an accurate
717 approximation of the SGS dissipation spectrum.

718 *A-priori* analyses of three variants of the DG-VMS approach have been carried out. We
719 have considered the small-small [1], Vreman [2], and all-all variants [3]. We have observed that
720 the Vreman approach provides an improved agreement with the SGS dissipation spectrum as
721 compared to the small-small variant at lower computational cost. A similar improvement has
722 been obtained for the all-all approach. It presents a lower computational cost while behaving
723 similarly to the Vreman variant although the model viscosity does not vanish when the solution
724 is completely represented by the large-resolved scales.

725 It has been also shown in this study that, when the ideal SGS dissipation acting on the
726 large-resolved scales is negligible, the best results for the DG-VMS approach are obtained for
727 a scale-fraction parameter of $\beta = 0.75$. All results have been shown to only mildly depend on
728 the polynomial degree for $p \geq 5$ and more marked differences are observed for lower values of
729 p which lead to different optimal values of β . We therefore suggest to employ a value of $p \geq 5$
730 as it leads to a more consistent behaviour of the ideal energy transfer mechanism and a good
731 agreement of the DG-VMS approach with the ideal quantities.

732 Finally, we have shown that the DG-VMS approach is not able to reproduce the viscous-type
733 behaviour observed at relatively low wavenumbers when the resolution limit falls within the
734 inertial range. Under these conditions, a mixed model based on the Smagorinsky model and the
735 DG-VMS approach with $\beta = 0.75$ can provide an improved agreement over a wide range of
736 resolutions provided that the model coefficients are dynamically adapted.

737 *Acknowledgments*

738 This project has received funding from the European Union's Horizon 2020 research and
739 innovation program under the Marie Skłodowska-Curie grant agreement No 675008. Part of
740 this research was conducted during the 2018 Center for Turbulence Research (CTR) Summer
741 Program at Stanford University. The second author would like to acknowledge funding from

742 CTR for participation in the Summer Program. This work was performed using HPC resources
 743 from CINES and TGCC (GENCI Grants 2017-A0022A10129, 2017-A0032A07624 and 2018-
 744 A0052A07624).

745 **Appendix A. Energy and dissipation spectra computation**

746 For the computation of the energy and dissipation spectra we need to evaluate the Fourier
 747 transform of the velocity field, SGS residual, and SGS model term. For this purpose we employ
 748 the Fast Fourier Transform (FFT) algorithm as implemented in the *FFTW-3.3.8* library [48].

749 The FFT algorithm requires the solution to be known on an uniform Cartesian grid. The
 750 variable of which we want to compute the FFT is therefore sampled on a post-processing grid
 751 formed by the union of n_{el}^3 uniform Cartesian grids centered on each cell and composed of q_s^3
 752 sampling points. The post-processing grid on the domain $[-\pi, \pi]^3$ is thus composed of the Carte-
 753 sian product of the coordinates $(j - \frac{1}{2}) \frac{2\pi}{q_s n_{el}}$ for $j = 1, \dots, N_{FFT} = q_s n_{el}$. The value of q_s must be
 754 sufficiently large to evaluate accurately the Fourier coefficients corresponding to the frequencies
 755 of interest (that is at least up to k_{DG}).

756 Indeed, the presence of discontinuities in the DG-LES field leads to a reduction in the order
 757 of convergence of the FFT algorithm. We remark that the FFT algorithm relies on the trapezoidal
 758 integration rule which presents an order of accuracy $O(N_{FFT}^{-1})$ in the presence of discontinuities,
 759 as opposed to the exponential convergence obtained for smooth functions. In this case the use of
 760 $n_{el}(p + 1)$ points per direction, as is usually found in the literature of DG-LES, is not sufficient
 761 for the evaluation of the energy and dissipation spectra. For this reason, we employ at least
 762 $3n_{el}(p + 1)$ points per direction and verify that increasing this value does not modify the energy
 763 and dissipation spectra at frequencies below k_{DG} .

764 In order to illustrate the need for a sufficiently high number of points for the evaluation of the
 765 FFT, we report in Fig. A.29 the energy spectra of the DG-LES solution of the TGV configuration
 766 at $Re = 20\,000$ and $t = 14$ using $p = 5$ and 7 and a total of 288 degrees of freedom for various
 767 values of q_s . It can be observed that the FFT is inaccurate for low values of q_s even at wavenum-
 768 bers below k_{DG} . Slight differences can be observed for frequencies below \tilde{k}_{DG} and in some cases
 769 marked differences can appear at frequencies close to k_{DG} . This is visible from the bump in the
 770 energy spectrum at k_{DG} for $q_s = p + 1$ on the right panel of Fig. A.29 corresponding to $p = 7$.

771 Nonetheless, the spectrum converges as q_s is increased and a value of $q_s \approx 3n_{el}(p + 1)$ ap-
 772 pears sufficient to obtain the Fourier transform for frequencies up to k_{DG} . Further increasing the
 773 value of q_s leads to the slow convergence of the tail of the spectrum associated with the DG-LES
 774 discontinuities.

775 We note that alternative techniques can be employed to evaluate the Fourier transform avoid-
 776 ing the use of a large number of post-processing points. Such methodologies include the Non
 777 Uniform Fast Fourier Transform (NUFFT) [49, 50] and the Conformal Fourier Transform (CFT)
 778 [51].

779 **Appendix B. Choice of the large-scale space**

780 In Sec. 3 we have defined the space $W_h^m = \text{span} \left\{ \psi_K^{\mathbf{m}}, \forall K \in \Omega_h, m - \frac{1}{2} < \|\mathbf{m}\| \leq m + \frac{1}{2} \right\}$. With
 781 this choice the assumption of $\tilde{T}_{sgs}(m) = 0$ for $m \leq p_L$ corresponds to the VMS approach defining
 782 the large-scale space as $V^L := \bigcup_{m \leq p_L} W_h^m$ as described in Sec. 4. Other definitions are possible,

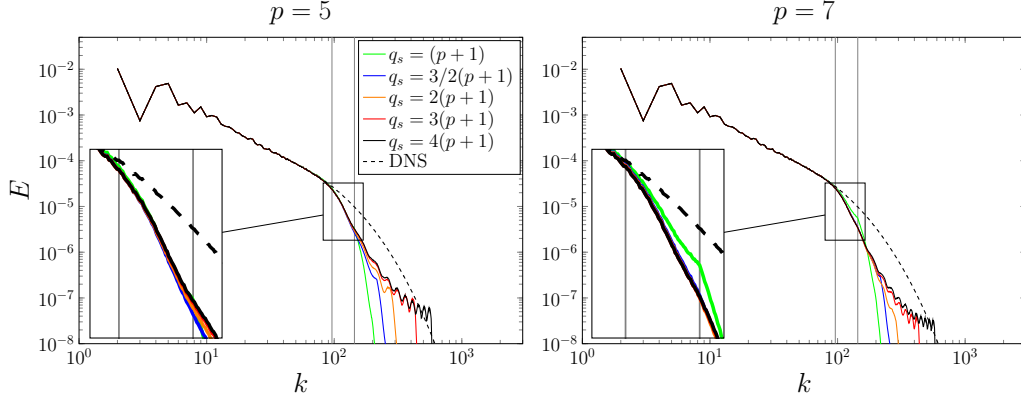


Figure A.29: TGV at $\text{Re} = 20\,000$, $t = 14$, $k_{\text{DG}} = 144$: Energy spectrum for $p = 5$ (left) and $p = 7$ (right) for various values of q_s .

783 in particular the most common choice is to define $V^L := S_h^{p_L}$ which corresponds to assuming that
 784 $\tilde{T}^c(m) = 0$ for $m \leq p_L$ where

$$\tilde{T}^c(m) := \mathcal{R}(\mathbf{u}, \bar{\mathbf{u}}_h, \mathbb{P}_{W_h^{m,c}}[\bar{\mathbf{u}}_h]), \quad (\text{B.1})$$

785 with $W_h^{m,c} = \text{span}\{\psi_K^{\mathbf{m}}, \forall K \in \Omega_h, \|\mathbf{m}\|_\infty = m\}$. It is immediate to show that $W_h^{m,c} \equiv S_h^m \setminus S_h^{m-1}$ for
 786 $m > 0$ and that $W_h^{0,c} \equiv S_h^0$.

787 The definition employed throughout this work Eq. (20) corresponds to analysing the modal
 788 energy transfer by grouping together modes over spherical shells characterized by $m - \frac{1}{2} <$
 789 $\|\mathbf{m}\| \leq m + \frac{1}{2}$, whereas Eq. (B.1) corresponds to grouping modes over cubic shells characterized
 790 by $\|\mathbf{m}\|_\infty = m$.

791 We argue that Eq. (20) allows for a more consistent description of the modal energy transfer
 792 mechanism. To justify this choice we report in Figs. B.30 and B.31 the contour plots of the modal
 793 eddy viscosity $\tilde{\nu}^\dagger(\mathbf{m})$ for $p = 7$ and $p = 11$ defined as

$$\tilde{\nu}^\dagger(\mathbf{m}) := \frac{\sum_{K \in \Omega_h} \tilde{\mathbf{u}}_h^{\mathbf{m},K} \cdot \mathcal{R}(\mathbf{u}, \bar{\mathbf{u}}_h, \psi_K^{\mathbf{m}})}{\sum_{K \in \Omega_h} \nu \tilde{\mathbf{u}}_h^{\mathbf{m},K} \cdot \mathcal{L}(\bar{\mathbf{u}}_h, \psi_K^{\mathbf{m}})}. \quad (\text{B.2})$$

794 We observe that the isolevel curves for $\tilde{\nu}^\dagger(\mathbf{m})$ are better approximated by spheres (circles in
 795 the plot) rather than by cubes centred in $(0, 0, 0)$. Therefore we assume that improved results can
 796 be obtained for LES models by modifying the modal eddy viscosity as a function of $\|\mathbf{m}\|$ rather
 797 than $\|\mathbf{m}\|_\infty$.

- 798 [1] T. J. Hughes, L. Mazzei, A. A. Oberai, A. A. Wray, The multiscale formulation of large eddy simulation: Decay of
 799 homogeneous isotropic turbulence, *Phys Fluids* 13 (2) (2001) 505–512.
 800 [2] A. Vreman, The filtering analog of the variational multiscale method in large-eddy simulation, *Phys Fluids* 15 (8)
 801 (2003) L61–L64.
 802 [3] J.-B. Chapelier, M. de la Llave Plata, E. Lamballais, Development of a multiscale LES model in the context of a
 803 modal discontinuous Galerkin method, *Comput Method Appl M* 307 (2016) 275–299.
 804 [4] R. S. Rogallo, P. Moin, Numerical simulation of turbulent flows, *Annu Rev Fluid Mech* 16 (1) (1984) 99–137.
 805 [5] M. Lesieur, O. Métais, P. Comte, *Large-eddy Simulations of Turbulence*, Cambridge University Press, 2005.

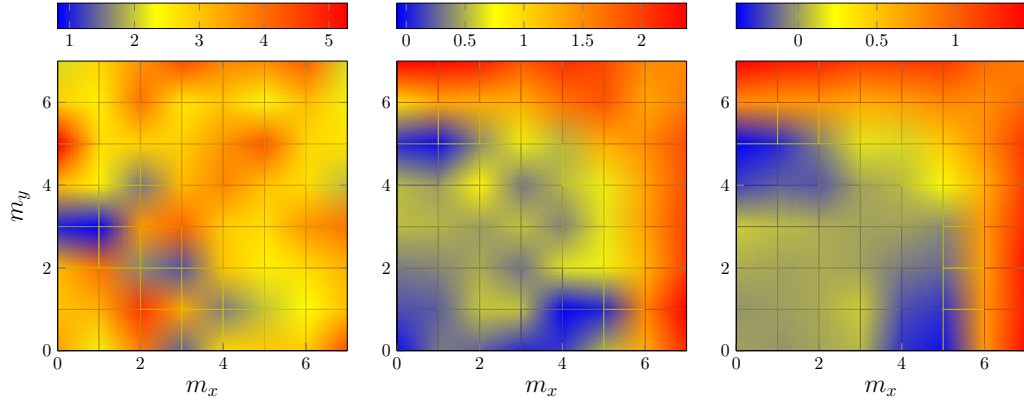


Figure B.30: TGV at $\text{Re} = 20,000$, $t = 14$: Contour plot of $\vec{v}^+(\mathbf{m})$ at constant $m_z = 0$ for $p = 7$ and 144^3 , 288^3 and 576^3 dofs (left to right) using the BR1 scheme.

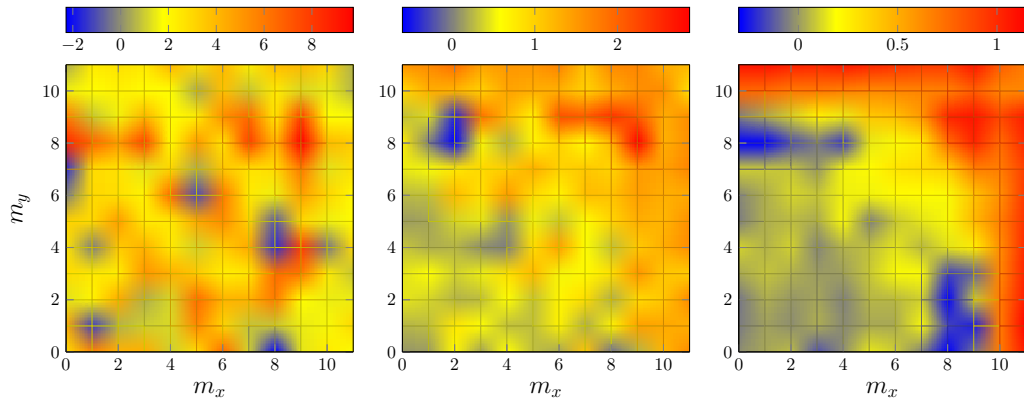


Figure B.31: TGV at $\text{Re} = 20,000$, $t = 14$: Contour plot of $\vec{v}^+(\mathbf{m})$ at constant $m_z = 0$ for $p = 11$ and 144^3 , 288^3 and 576^3 dofs (left to right) using the BR1 scheme.

- 806 [6] P. Sagaut, Large eddy simulation for incompressible flows: an introduction, Springer Science & Business Media,
807 2006.
- 808 [7] W. Heisenberg, On the theory of statistical and isotropic turbulence, P Roy Soc Lond A Mat 195 (1042) (1948)
809 402–406.
- 810 [8] R. H. Kraichnan, Eddy viscosity in two and three dimensions, J Atmos Sci 33 (1976) 1521–1536.
- 811 [9] J. A. Domaradzki, W. Liu, M. E. Brachet, An analysis of subgrid-scale interactions in numerically simulated
812 isotropic turbulence, Phys Fluids A 5 (1993) 1747–1759.
- 813 [10] D. McComb, A. Young, Explicit-scales projections of the partitioned non-linear term in direct numerical simulation
814 of the Navier-Stokes equation, in: Second Monte Verita Colloquium on Fundamental Problematic Issues in Fluid
815 Turbulence, 1998.
- 816 [11] O. Métais, M. Lesieur, Spectral large-eddy simulation of isotropic and stably stratified turbulence, J Fluid Mech
817 239 (1992) 157–194.
- 818 [12] J. Smagorinsky, General circulation experiments with the primitive equations: I. the basic experiment, Mon Weather
819 Rev 91 (3) (1963) 99–164.
- 820 [13] H. Jeanmart, G. Winckelmans, Investigation of eddy-viscosity models modified using discrete filters: A simplified
821 regularized variational multiscale model and an enhanced field model, Phys Fluids 19 (5) (2007) 055110.
- 822 [14] M. Germano, U. Piomelli, P. Moin, W. H. Cabot, A dynamic subgrid-scale eddy viscosity model, Phys Fluids A:
823 Fluid 3 (7) (1991) 1760–1765.
- 824 [15] T. J. R. Hughes, G. N. Wells, A. A. Wray, Energy transfers and spectral eddy viscosity in large-eddy simulations
825 of homogeneous isotropic turbulence: Comparison of dynamic Smagorinsky and multiscale models over a range
826 of discretizations, Phys Fluids 16 (11) (2004) 4044–4052.
- 827 [16] T. J. R. Hughes, L. Mazzei, K. E. Jansen, Large eddy simulation and the variational multiscale method, Comput Vi-
828 sualization Sci 3 (2000) 47–59.
- 829 [17] V. Gravemeier, The variational multiscale method for laminar and turbulent flow, Arch Comput Method E 13 (2)
830 (2006) 249.
- 831 [18] N. Ahmed, T. Chacón Rebollo, V. John, S. Rubino, A review of Variational Multiscale Methods for the simulation
832 of turbulent incompressible flows, Arch Comput Method E 24 (2017) 115–164.
- 833 [19] U. Rasthofer, V. Gravemeier, Recent developments in Variational Multiscale Methods for Large-Eddy Simulation
834 of turbulent flow, Arch Comput Method E (2017) 1–44.
- 835 [20] S. S. Collis, Monitoring unresolved scales in multiscale turbulence modeling, Phys Fluids 13 (6) (2001) 1800–1806.
- 836 [21] B. Cockburn, C.-W. Shu, Runge–Kutta Discontinuous Galerkin Methods for Convection-Dominated Problems, J
837 Sci Comput 16 (3) (2001) 173–261. doi:10.1023/A:1012873910884.
838 URL <https://doi.org/10.1023/A:1012873910884>
- 839 [22] D. Leslie, G. Quarini, The application of turbulence theory to the formulation of subgrid modelling procedures, J
840 Fluid Mech 91 (1) (1979) 65–91.
- 841 [23] S. Cerutti, C. Meneveau, O. M. Knio, Spectral and hyper eddy viscosity in high-Reynolds-number turbulence, J
842 Fluid Mech 421 (2000) 307–338.
- 843 [24] E. Lamballais, T. Dairay, S. Laizet, J. Vassilicos, Implicit/Explicit Spectral Viscosity and Large-Scale SGS Effects,
844 in: Direct and Large-Eddy Simulation XI, Springer, 2019, pp. 107–113.
- 845 [25] J. Holmen, T. J. Hughes, A. A. Oberai, G. N. Wells, Sensitivity of the scale partition for variational multiscale
846 large-eddy simulation of channel flow, Phys Fluids 16 (3) (2004) 824–827.
- 847 [26] S. Ramakrishnan, S. S. Collis, Partition selection in multiscale turbulence modeling, Phys Fluids 18 (2006) 075105.
- 848 [27] P. Sagaut, V. Levasseur, Sensitivity of spectral variational multiscale methods for large-eddy simulation of isotropic
849 turbulence, Phys Fluids 17 (2005) 035113.
- 850 [28] J. Meyers, P. Sagaut, Evaluation of smagorinsky variants in large-eddy simulations of wall-resolved plane channel
851 flows, Phys Fluids 19 (9) (2007) 095105.
- 852 [29] D. K. Lilly, The representation of small-scale turbulence in numerical simulation experiments, in: IBM Scientific
853 Computing Symposium on Environmental Sciences, 1966.
- 854 [30] J. Meyers, P. Sagaut, On the model coefficients for the standard and the variational multi-scale Smagorinsky model,
855 J Fluid Mech 569 (2006) 287–319.
- 856 [31] S. Pope, Large-eddy simulation using projection onto local basis functions, in: Lect Notes Phys, Springer, 2001,
857 pp. 239–265.
- 858 [32] A. Vreman, The adjoint filter operator in large-eddy simulation of turbulent flow, Phys Fluids 16 (6) (2004) 2012–
859 2022.
- 860 [33] S. Collis, The DG/VMS method for unified turbulence simulation, in: 32nd AIAA Fluid Dynamics Conference and
861 Exhibit, 2002, p. 3124.
- 862 [34] A. D. Beck, D. G. Flad, C.-D. Munz, Neural networks for data-based turbulence models, arXiv preprint
863 arXiv:1806.04482 (2018).
- 864 [35] F. van der Bos, B. J. Geurts, Computational error-analysis of a discontinuous galerkin discretization applied to

- 865 large-eddy simulation of homogeneous turbulence, *Comput Method Appl M* 199 (13-16) (2010) 903–915.
- 866 [36] D. Gottlieb, S. A. Orszag, *Numerical analysis of spectral methods: theory and applications*, Vol. 26, Siam, 1977.
- 867 [37] G. Karamanos, G. E. Karniadakis, A spectral vanishing viscosity method for large-eddy simulations, *J Comput*
868 *Phys* 163 (1) (2000) 22–50.
- 869 [38] A. A. Oberai, V. Gravemeier, B. G. C., Transfer of Energy in the variational multiscale formulation of LES, in:
870 *Proceedings of the 2004 Summer Program*, 2004.
- 871 [39] F. Bassi, S. Rebay, A high-order accurate discontinuous finite element method for the numerical solution of the
872 compressible navier–stokes equations, *J Comput Phys* 131 (2) (1997) 267–279.
- 873 [40] F. Bassi, A. Crivellini, S. Rebay, M. Savini, Discontinuous Galerkin solution of the Reynolds-averaged Navier–
874 Stokes and $k-\omega$ turbulence model equations, *Comput Fluids* 34 (4-5) (2005) 507–540.
- 875 [41] D. Flad, G. Gassner, On the use of kinetic energy preserving DG-schemes for large eddy simulation, *J Comput*
876 *Phys* 350 (2017) 782–795.
- 877 [42] S. Stolz, P. Schlatter, L. Kleiser, High-pass filtered eddy-viscosity models for large-eddy simulations of transitional
878 and turbulent flow, *Phys Fluids* 17 (6) (2005) 065103.
- 879 [43] R. C. Moura, G. Mengaldo, J. Peiró, S. Sherwin, On the eddy-resolving capability of high-order discontinuous
880 Galerkin approaches to implicit LES/under-resolved DNS of Euler turbulence, *J Comput Phys* 330 (2017) 615–
881 623.
- 882 [44] J. Meyers, P. Sagaut, B. J. Geurts, Optimal model parameters for multi-objective large-eddy simulations, *Phys*
883 *Fluids* 18 (9) (2006) 095103.
- 884 [45] M. Alhawwary, Z. Wang, On the accuracy and stability of various dg formulations for diffusion, arXiv preprint
885 arXiv:1810.03095 (2018).
- 886 [46] F. Naddei, M. de la Llave Plata, E. Lamballais, V. Couaillier, M. Massot, M. Ihme, Large-scale space definition for
887 the DG-VMS method based on energy transfer analyses, in: *Proceedings of the 2018 Summer Program*, 2018.
- 888 [47] Z. Wang, A. Oberai, A mixed large eddy simulation model based on the residual-based variational multiscale
889 formulation, *Phys Fluids* 22 (7) (2010) 075107.
- 890 [48] M. Frigo, S. G. Johnson, The design and implementation of FFTW3, *Proceedings of the IEEE* 93 (2) (2005) 216–
891 231, special issue on “Program Generation, Optimization, and Platform Adaptation”.
- 892 [49] J.-Y. Lee, L. Greengard, The type 3 nonuniform FFT and its applications, *J Comput Phys* 206 (1) (2005) 1–5.
- 893 [50] G.-X. Fan, Q. H. Liu, Fast Fourier transform for discontinuous functions, *IEEE T Antenn Propag* 52 (2) (2004)
894 461–465.
- 895 [51] C.-H. Zhu, Q. H. Liu, Y. Shen, L. Liu, A high accuracy conformal method for evaluating the discontinuous fourier
896 transform, *Prog Electromagn Res* 109 (2010) 425–440.